

# Gamma-ray production cross sections in proton interactions with $^{nat}\text{Mg}$ , $^{nat}\text{Si}$ and $^{56}\text{Fe}$ targets: measurement over the energy range of $E_p = 66 - 125$ MeV, data analysis, results and discussion. Astrophysical implications.

M. Debabi<sup>1</sup>, S. Ouichaoui<sup>1\*</sup>, A. Belhout<sup>1</sup>, J. Kiener<sup>2</sup>, E. A. Lawrie<sup>3</sup>, J. J. Lawrie<sup>3</sup>, D. Moussa<sup>1</sup>, W. Yahia-Cherif<sup>3</sup>, Y. Rahma<sup>4</sup>, V. Tatischeff<sup>2</sup>, V., H. Benhabiles-Mezhoud<sup>5</sup>, T. D. Bucher<sup>3</sup>, A. Chafa<sup>1</sup>, L. J. Conradie<sup>3</sup>, S. Damache<sup>4</sup>, I. Deloncle<sup>2</sup>, J. L. Easton<sup>6</sup>, C. Hamadache<sup>2</sup>, F. Hammache<sup>7</sup>, P. Jones<sup>3</sup>, V. B. Kheswa<sup>8</sup>, N. A. Khumalo<sup>9</sup>, A. Kunyana<sup>10</sup>, T. Lamula<sup>9</sup>, S. N. T. Majola<sup>11</sup>, J. Ndayishimye<sup>8</sup>, D. Negi<sup>3</sup>, S. P. Noncolela<sup>9</sup>, S. Ouziane<sup>1</sup>, P. Papka<sup>5</sup>, N. de Séréville<sup>7</sup>, J. F. Sharpey-Schafer<sup>9</sup>, O. Shirinda<sup>8</sup>, A. Trabelsi<sup>4</sup>, M. Wiedeking<sup>3</sup>, and S. Wyngaardt<sup>8</sup>

<sup>1</sup>University of Sciences and Technology Houari Boumediene (USTHB), Laboratory of Nuclear Sciences and Radiation-Matter Interactions (SNIRM-DGRSDT), Faculty of Physics, P.O. Box 32, EL Alia, 16111 Bab Ezzouar, Algiers, Algeria

<sup>2</sup>Centre de Sciences Nucléaires et de Sciences de la Matière (CSNSM), CNRS-IN2P3 et Université de Paris-Sud, 91405 Orsay Campus, France

<sup>3</sup>iThemba LABS, National Research Foundation, P.O. Box 722, Somerset West 7129, South Africa

<sup>4</sup>CRNA, 02 Boulevard Frantz Fanon, B.P. 399 Alger-gare, Algiers, Algeria

<sup>5</sup>Université M'Hamed Bougara, Institut de Génie Electrique et Electronique, 35 000 Boumerdés, Algeria

<sup>6</sup>Department of Physics, University of the Western Cape, Private Bag X17, Bellville 7535, South Africa

<sup>7</sup>Institut de Physique Nucléaire (IPN), CNRS-IN2P3 et Université Paris-Sud, 91405 Orsay Campus, France

<sup>8</sup>Department of Physics, Stellenbosch University, Private Bag X1, Matieland 7602, South Africa

<sup>9</sup>Department of Physics, University of the Western Cape, Private Bag X17, Bellville 7535, South Africa

<sup>10</sup>Department of Physics and Engineering University of Zululand Private Bag X1001, Kwa-Dlangezwa 3886 South Africa

<sup>11</sup>Department of Physics, University of Cape Town, Private Bag X3, 7701 Rondebosch, South Africa

## Abstract:

We have measured nuclear  $\gamma$ -ray line production cross sections in interactions of highly accelerated proton beams with various target nuclei abundant in astrophysical sites. The experiments were carried out at the 200-MV Separated Sector Cyclotron (SSC) of iThemba LABS (near Cape Town, in South Africa) using a high-energy resolution and high efficiency detection system for registering the emitted  $\gamma$ -ray photons. We report and discuss in this paper the collected experimental data sets for various  $\gamma$ -ray lines produced in bombarding  $^{nat}\text{Mg}$ ,  $^{nat}\text{Si}$  and  $^{56}\text{Fe}$  targets with proton beams of incident energies of  $E_p = 66, 80, 95, 110$  and  $125$  MeV. After describing the experimental set up and the data analysis method used, we report and discuss our total experimental cross section results in comparisons to previous counterparts from the literature, to a semi-empirical compilation and to the predictions of nuclear reaction theory via performed TALYS code calculations. Significantly improved agreements between theory and experiment are point out when using our modified optical model potential and  $\beta_\lambda$  level deformation parameters instead of the default input parameters built in TALYS.

Finally, we put into perspective the applications of our results in nuclear physics and astrophysics with drawing relevant conclusions.

Keywords: Proton-induced nuclear reactions;  $\gamma$ -ray production cross sections;  $\gamma$ -ray spectrometry;  $\gamma$ -ray spectroscopy; Astrophysical implications

## 1. Introduction

Nuclear  $\gamma$ -ray production cross sections in interactions of highly accelerated particles (protons, deuterons,  $^3\text{He}^+$  ions,  $\alpha$ -particles) with atomic nuclei are needed for several purposes in various scientific research fields such as proton therapy, materials science,  $\gamma$ -ray astronomy and astrophysics. In particular, measuring these observables at ground laboratory accelerators has great importance to the latter two disciplines for simulating and modeling the  $\gamma$ -ray line emission in astrophysical sites like the solar flares (SFs), the galactic center, the interstellar medium (ISM), supernovae remnants and cosmic compact objects (pulsars, quasars, active galactic nuclei, etc.). The obtained results can allow the subsequent validation of observational data reported by space telescopes like the e-ASTROGAM [1,2], FERMI [3] and precursor missions (SMM [4,5], CGRO [5], RHESSI [6] and INTEGRAL [7, 8]).

Under non-thermal acceleration by strong magnetic fields in astrophysical sites, the charged particles can reach very high energies of several hundreds GeV/u. They violently interact with abundant elements (H, He, C, N, O, Ne, Mg, Al, Si, S, Ca and Fe), giving rise to various nuclear reaction processes including the de-excitations of synthesized radioactive nuclei and excited nuclei upon having undergone inelastic particle scattering and other nuclear reactions (nucleon transfer, charge-exchange, pre-equilibrium or spallation reactions). These reaction processes produce discrete  $\gamma$ -ray lines that can provide valuable information on the composition of the accelerating media and the properties of the accelerated particles (their nature, sources, spatial distribution, energy spectra and relative abundances) [9 - 13] as for, e.g., the low-energy cosmic rays (LECRs) permanently bombarding the inner galaxy, which are elusive to direct observation due to their deviation and spreading by the solar winds within the solar system. This is particularly the case of protons and  $\alpha$ -particles from SFs and the ISM, whose energies extend from the nuclear reaction thresholds up to very high values out of reach in ground laboratory ion accelerators. The most important nuclear reactions are those induced by these particles on heavier nuclei of abundant chemical elements, and the inverse reactions induced by the accelerated ions of these elements on the dominant Hydrogen and Helium [14–18]. Three specific  $\gamma$ -ray line components have been identified [19] in the observed  $\gamma$ -ray emission spectra from SFs and the ISM, consisting in a narrow and a broad components of strong, discrete  $\gamma$ -ray lines, and a non-resolved component of weak lines in form of a quasi-continuum emitted by highly excited nuclear states.

Therefore, laboratory measurements of  $\gamma$ -ray line production cross sections over as wide as possible particle energy domains is required for elucidating the complex nuclear reaction processes at work in astrophysical sites and well understanding the subsequent  $\gamma$ -ray emission and related complex energy spectra.

Previous measurements of these observables have been carried out mainly at the Washington [20-23] and Orsay Paris-Saclay [17, 24-28] universities tandem accelerators for protons and  $\alpha$ -particles of incident energies reaching values of  $E_p = 26$  and  $E_\alpha = 40$  MeV. Cross section experimental data for some strong lines have also been taken [29] at the Lawrence Berkeley Laboratory's 88-Inch cyclotron accelerators for these particles accelerated respectively up to  $E_p = 50$  MeV and  $E_\alpha = 40$  MeV. More recently, Kiener et al. [30] extended the experimental data for the strongest  $\gamma$ -ray lines produced in  $\alpha$ -particle induced reactions on C, Mg, Si and Fe targets over the incident energy range of  $E_\alpha = 50 - 90$  MeV at the Berlin's Helmholtz-Zentrum cyclotron accelerator.

Besides, a semi-empirical compilation exists [31] consisting in a collection of available in 2009 experimental data for strong  $\gamma$ -ray lines prominent in SFs and the ISM. It also predicts their production cross sections at higher particle energies not covered by experiment based only on TALYS code [32] calculations.

In this context, we have undertaken an experimental campaign in joint scientific collaboration (see Ref. [18]) aiming at measuring  $\gamma$ -ray line production cross sections at the 200-MV SSC facility of iThemba LABS. We have investigated a collection of solid targets of elements  $^{nat}\text{C}$ , C and O within Mylar,  $^{nat}\text{Mg}$ ,  $^{nat}\text{Si}$ ,  $^{40}\text{Ca}$  and  $^{56}\text{Fe}$  under bombardment of high-energy proton beams. Given that earlier experimental data sets were available mainly for proton energies of  $E_p \cong 26$  MeV [17, 20-28], we explored the remaining higher energy region of  $E_p = 30 - 200$  MeV allowed by the SSC accelerator. We successively carried out measurements at three separate proton energy ranges of  $E_p = 30 - 66$  MeV in 2014,  $E_p = 66 - 125$  MeV in 2015 and  $E_p = 125 - 200$  MeV in 2016 using the AFRODITE Germanium array [33-35] for detecting the emitted  $\gamma$ -rays. In performing this program, the measurements at the proton boundary energies of  $E_p = 66$  and 125 MeV were repeated for the sake of data checking and validation. Part of the measured nuclear  $\gamma$ -ray line production cross sections has been the subject of recent publications by our collaboration [18, 36-39]. In particular, in Ref. [18] we extended earlier experimental data for main, intense  $\gamma$ -ray lines from the  $^{nat}\text{Mg}$ ,  $^{nat}\text{Si}$  and  $^{56}\text{Fe}$  targets to higher proton energies up to  $E_p = 66$  MeV and reported new other data for weaker lines. In Ref. [36] we reported new production cross section experimental data for de-

excitation lines produced in proton-induced nuclear reactions on  $^{nat}\text{C}$  and Mylar targets over the incident energy range of  $E_p = 30 - 200$  MeV.

In the present paper, we report on new cross section experimental data for  $\gamma$ -ray lines produced in interactions of 66, 80, 95, 110 and 125 MeV proton beams with  $^{nat}\text{Mg}$ ,  $^{nat}\text{Si}$  and  $^{56}\text{Fe}$  targets. In the following, we first present the experimental set-up and methods used in section 2, then our procedure of data analysis in section 3. The derived experimental results are reported in Section 4 where the total integrated  $\gamma$ -ray cross sections are discussed in comparison to counterpart data sets from the literature [17, 18, 24, 25, 29] and to the Murphy et al. semi-empirical compilation [31].

In section 5, we discuss our total cross section experimental results within the predictions of nuclear reaction theory via performed comprehensive TALYS code [32] calculations. Finally, we discuss in section 6 the astrophysical implications of our results with tracing perspectives and drawing conclusions.

## 2. Experimental set-up and methods

Detailed descriptions of the experimental set-up and methods used in our experiments have been provided in our previous papers (18, 36). Therefore, we limit ourselves here to present the main related information.

Proton beams of energies  $E_p = 66, 80, 95, 110, 125$  MeV and current intensities  $I = 2 - 5$  nA delivered by the SSC accelerator were directed onto self-supporting solid targets of  $^{nat}\text{Si}$ ,  $^{nat}\text{Mg}$  and  $^{56}\text{Fe}$  of thicknesses lying within the range of 5-9 mg/cm<sup>2</sup>. Table 1 lists the explored targets and reports their characteristics and the corresponding bombarding proton beam energies used.

Table 1: target properties and proton beam energies correspondingly used.

Target	Thickness (mg/cm <sup>2</sup> )	Purity (%)	Proton energies $E_p$ (MeV)	References
Mg	$5 \pm 0.02$	Natural <sup>a</sup>	66, 80, 95 and 110	[11-14]
	$8.99 \pm 0.04$	Natural	125	
Si	$5.82(6) \pm 0.04$	Natural <sup>b</sup>	80, 95 and 110	[11,12, 15, 16]
	$5.00 \pm 0.3$	Natural	66 and 125	
Fe	$7.40 \pm 0.37$	$^{56}\text{Fe}(>99\%)$	66, 80, 95, 110, 125	[11-14]
	$5.50 \pm 0.08$	$^{56}\text{Fe}(>99\%)$	125	

<sup>a</sup>Isotopic composition of  $^{nat}\text{Mg} = ^{24}\text{Mg}$  (78.99%) +  $^{25}\text{Mg}$  (10%) +  $^{26}\text{Mg}$  (11.01%)

<sup>b</sup>Isotopic composition of  $^{nat}\text{Si} = ^{28}\text{Si}$  (92.22%)+ $^{29}\text{Si}$  (4.68%)+ $^{30}\text{Si}$  (3.09%)

The purity of the targets in other contaminants before the proton irradiations was higher than 99.99%. The targets were mounted onto rectangular Al frames, then fixed on a common Al ladder. The latter was equipped with a fluorescent Al<sub>2</sub>O<sub>3</sub> viewer serving for tuning the particle beam and an empty-target frame devoted to measure the beam-induced  $\gamma$ -ray and neutron backgrounds.

The integrated beam current was measured to within 1% uncertainty by means of a well-designed, well-protected and electrically isolated Faraday cup located 3 meters away behind a concrete wall. The collected beam charge amounted typically to  $\approx 5 \mu\text{C}$  for 1-hour duration runs. The AFRODITE Ge array, composed of 8 clovers of the EUROGAM-phase II type [40] was used in a fixed geometry for detecting the emitted  $\gamma$ -ray photons. Each clover contained 4 HP-Ge crystals of the n-type, each having an area of  $50 \times 70 \text{ mm}^2$ . One of the main advantages of the Clover detectors lies in their ability to reduce the Doppler-broadening effects owing to their compact geometry and small opening angle, which significantly enhances their energy resolution in comparison to larger volume detectors. The HP-Ge crystals, shielded by means of Compton-suppressing BGO crystals, were housed into a common cryostat. The whole detection system subtended a large solid angle amounting to  $\sim 7.5\%$  of the total  $4\pi \text{ sr}$  sphere. In general, four clovers were placed at laboratory angles of  $90^\circ$ , while the other four were set at  $\theta_{\text{lab}} = 135^\circ$  relative to the incident beam direction (see, e.g., Fig. 1 in Ref. [36]). The HP-Ge crystals in each clover were set symmetrically at  $\pm 5^\circ$  relative to its center. This configuration of the detection array thus involving 32 HP-Ge crystals allowed us to measure  $\gamma$ -ray angular distributions with only four observation angles each, i.e.,  $\theta_{\text{lab}} = 85^\circ, 95^\circ, 130^\circ$  and  $140^\circ$ . It was also possible to place clover detectors forward at  $\theta_{\text{lab}} = 45^\circ$  relative to the incident beam direction. However, we avoided using these detection positions in order to protect the HP-Ge crystals against probable damages due to expected high neutron fluxes from proton-induced nuclear reactions on the targets and the (Al, Ge) elements composing the surrounding materials (beam pipe, reaction chamber, HP-Ge detectors).

The proton beam energies were accurately determined via performing careful energy calibrations of the AFRODITE detection array. We used calibrated standard radioactive sources of  $^{60}\text{Co}$ ,  $^{137}\text{Cs}$  and  $^{152}\text{Eu}$  for covering the  $\gamma$ -ray low-energy range of  $E_\gamma = (0.122 - 1.408) \text{ MeV}$  and, sometimes, a  $^{56}\text{Co}$  source for extending this energy range up to  $E_\gamma \approx 3 \text{ MeV}$ . We also used the strong  $\gamma$ -ray line of  $^{16}\text{O}$  at  $6.129 \text{ MeV}$  and its associated escape lines at  $E_\gamma = 5.107$  and  $5.618 \text{ MeV}$  produced in the  $^{16}\text{O} (p, p'\gamma)$  inelastic proton scattering from a Mylar

target. The relative energy resolution,  $\Delta E_\gamma/E_\gamma$ , frequently determined relative to the line of  $^{60}\text{Co}$  at  $E = 1332$  keV, amounted to less than 0.20 %.

The same radioactive sources mentioned above were also used for measuring the absolute detection efficiency,  $\varepsilon(E_\gamma, \theta)$ , versus the photon energy up to  $E_\gamma = 1.408$  MeV and observation angle. Its values at fixed angle  $\theta$  were determined by the relation

$$\varepsilon(E_\gamma) = \frac{N(E)}{A(t) \times t \times I} \quad (1)$$

from the count rates (photopeak areas) in the  $\gamma$ -ray energy spectra,  $N(E)$ , the source activities at the measurement time,  $A(t)$ , the acquisition time interval,  $t$ , and the  $\gamma$ -ray branching ratios,  $I$ , and were regularly checked during all the experiments. We extended further this  $\gamma$ -ray energy range up to  $E_\gamma = 3.5$  MeV using efficiency values from a previous experiment [41] performed with a  $^{56}\text{Co}$  radioactive source in similar conditions to our measurements that we normalized to our experimental data. The systematic uncertainty in this normalization amounted to less than 2% based on the deviation in the region of overlap between the experimental data sets.

We systematically recorded  $\gamma$ -ray background energy spectra from various sources (the explored targets, experimental room, empty-target frame and surrounding materials). Then, we used them to correct the count rates in the  $\gamma$ -ray energy spectra from the nuclear reactions of interest in this study. The  $\gamma$ -ray count rates did not exceed 5-6 kHz per HP-Ge crystal; they were lower than 0.5 kHz during the runs performed with the beam passing through the empty-target frame. The beam current intensities did not exceed 5-6 nA in practically all the experimental runs, while the measured counting dead times were lying within the range of 6-8%.

A multi-instance data acquisition system (MIDAS [42]), composed of digital electronics modules made of XIA type ‘‘DGF Pixie-16’’, was used for collecting and storing the measured raw  $\gamma$ -ray energy spectra. The beforehand fixed experimental conditions were maintained stable with regularly tuning the proton beam, frequently monitoring the data acquisition system and checking the levels of the  $\gamma$ -ray and neutron backgrounds (see Refs. [18, 36]. Whence variations occurred in the prefixed experimental conditions, we further tuned the proton beam and adjusted its settings. Finally, we saved the measured  $\gamma$ -ray energy spectra and related time information onto compact discs for the sake of subsequent off-line data analyses after the experiments.

### 3. Data analysis

The different steps in the treatment and analysis of the recorded experimental data ( $\gamma$ -ray energy spectra, their precise energy calibration,  $\gamma$ -ray efficiencies) aim at determining as accurately as possible the  $\gamma$ -ray differential cross sections and the angle-integrated production cross sections. The analysis of the observed  $\gamma$ -ray line peaks of interest was carried out following the method detailed in Refs. [18, 24, 25, 36] that we applied to the 32 HP-Ge detectors used in our experiments. During the phase of data analysis following the experiments, we corrected the count rates within the raw  $\gamma$ -ray energy spectra for background events and dead time losses. We subtracted the beam-induced background by removing the count rates measured with the proton beam passing through the empty-target frame after proper normalization to the same beam charge. The data analysis can be proceeded via two distinct modes: (i) the direct, *single mode* considering each HP-Ge crystal as an individual detector and (ii) the *add-back mode* consisting in summing the count rates from two adjacent HP-Ge crystals of the same clover. Given that the counting rate statistics in the  $\gamma$ -ray energy spectra was high enough, we have used the former mode for extracting the contents of the observed  $\gamma$ -ray line peaks of interest. Normally, the Compton scattering background was supposed to be well suppressed by means of the shielding BGO crystals. However, for improving the suppression of this background component we additionally rejected all the  $\gamma$ -ray events observed in coincidence by the HP-Ge crystals of each clover detector. We used the ROOT [43] program and/or the GF3 software available in the RADWARE package [44] for extracting the line peak count rates in the useful  $\gamma$ -ray energy spectra. In general, when the  $\gamma$ -ray peaks were well defined and isolated as in the case of the energy spectra from the  $^{56}\text{Fe}$  target, we simply fitted symmetric Gaussian-shape distributions for extracting their content data (peak areas) with subtracting the related background by means of linear functions. However, a more elaborated multi-peak analysis method was applied in case of more complex, overlapping or significantly Doppler-broadened  $\gamma$ -ray line peaks as in case of the spectra from the  $^{\text{nat}}\text{Mg}$  and  $^{\text{nat}}\text{Si}$  targets. We evaluated the total relative uncertainties in the  $\gamma$ -ray line peak areas in form of three complementary contributions: (i) the systematic uncertainties, estimated to amount to 1 - 2% for strong line peaks and to 8 - 10% for least intense line peaks, (ii) the statistical uncertainties amounting to less than 2%, and (iii) the uncertainties in the fitting procedure not exceeding 3%. As we did during the experiments, along the subsequent data analysis phase we regularly checked the consistency of the derived values of the experimental  $\gamma$ -ray cross sections with corresponding counterparts predicted by the TALYS code.

As will be shown below in this section, the determination of the experimental  $\gamma$ -ray production cross sections requires the precise knowledge of the absolute detection efficiencies

over an extended  $\gamma$ -ray energy interval. Therefore, we further extrapolated the measured values of  $\varepsilon(E\gamma, \theta)$  by means of the radioactive sources up to  $E_\gamma \sim 10$  MeV via performing detailed Monte-Carlo simulations of the AFRODITE reaction chamber, the associated clover detection array and the surrounding materials using the GEANT4 software [45]. These simulations were made at the radioactive source energies and for regular  $\gamma$ -ray energy intervals between  $E_\gamma = 80$  keV and  $E_\gamma = 10$  MeV. Then, we normalized the simulated  $\varepsilon(E\gamma, \theta)$  values to the experimental data taken by means of the calibrated radioactive sources over the lower photon energy range. Furthermore, we fitted the following multi-parametric function

$$\varepsilon(E_\gamma, \theta) = e^{[(A+BX+CX^2)^{-G} + (D+EY+FY^2)^{-G}]^{-1/G}} \quad (2)$$

reported in the RADWARE software package [44] to the derived  $\varepsilon(E\gamma, \theta)$  data (see also Refs. [18, 36]).

In this expression,  $X = \log(E_\gamma/100)$ ,  $Y = \log(E_\gamma/1000)$ , and the the A, B, C, D, E, F coefficients are free adjustable parameters; the A, B, C coefficients describe the efficiency at low photon energies, the D, E, F ones describe the efficiency at higher photon energies, while the parameter G connects these two photon energy regions and controls the efficiency over the transition zone. Finally, we retained the resulting fitted curves to the data as the effective absolute detection efficiency values that were used for calculating the  $\gamma$ -ray line production cross sections as shown below.

Indeed, the experimental  $\gamma$ -ray differential cross sections (angular distributions) were calculated using the following equation

$$\frac{d\sigma(E_\gamma, \theta)}{d\Omega} = \frac{N(E_\gamma, \theta)}{\varepsilon(E_\gamma, \theta) N_t N_p} 10^{27} \text{ (mb/sr)} \quad (3)$$

in terms of the  $\gamma$ -ray line peak count rates,  $N_\gamma(E_\gamma, \theta)$ , the absolute detection efficiencies,  $\varepsilon(E_\gamma, \theta)$ , the target thicknesses,  $N_t$  (numbers of nuclei per  $\text{cm}^2$ ) and the numbers of projectiles hitting the targets,  $N_p$ . Then, we fitted a Legendre polynomial least-squares expansion of the form

$$W(\theta) = \sum_{\ell=0}^{\ell=\max} a_\ell Q_\ell P_\ell(\cos(\theta)) \quad (4)$$

to the differential cross section data. In this expression, the summation extends only over even integer  $\ell$ -values,  $\ell_{\max} = 2\lambda$  or  $2J$  with  $\lambda$  and  $J$  being respectively the  $\gamma$ -ray multipolarity and the spin of the emitting nuclear state, and the  $Q_\ell(\varepsilon, \ell, \theta)$  are energy-dependent geometrical attenuation coefficients [46, 47] introduced for taking into account the finite dimensions of

the  $\gamma$ -ray detectors and better evaluating the angular distribution expansion. We determined the latter coefficients via GEANT4 [45] Monte-Carlo simulations of the AFRODITE Ge detection array, finding nearly constant values of around unity over the whole photon energy range  $0.1 \text{ MeV} \leq E_\gamma \leq 10 \text{ MeV}$  of interest with relative uncertainties of  $\sim 1\%$ . Except for two M3  $\gamma$ -ray lines at 425.81 and 472.20 keV originating, respectively, from isomeric states in  $^{24}\text{Al}$  and  $^{24}\text{Na}$ , the observed  $\gamma$ -ray transitions have  $\lambda$ -values of at most 2 (see next subsection), which led us to fix  $\ell_{\max} = 4$  in Eq. (4). For the former two transitions in  $^{24}\text{Al}$  and  $^{24}\text{Na}$ , we restricted the expansion to the zeroth order term, given that the long lifetimes of the isomeric states lead to nuclear de-orientation of the aligned states resulting in isotropic angular distributions [18].

Finally, we determined the total, angle-integrated  $\gamma$ -ray line production cross sections only in terms of the  $a_0$  coefficients of the polynomial expansion given by Eq. (4), as indicated later in subsection 4.4.

## 4. Experimental results and discussion

### 4.1 $\gamma$ -ray energy spectra, nuclear transitions

Thanks to the meticulous energy calibration of the AFRODITE Ge detection array, we performed precise identifications of the  $\gamma$ -ray line peaks with total absolute uncertainties amounting typically to less than 0.1 keV. The recorded  $\gamma$ -ray energy spectra at different proton beam energies showed great similarities in their shapes ( $\gamma$ -ray lines + backgrounds) and the presence of an intense  $\gamma$ -ray background line at  $E_p = 511 \text{ keV}$  from the ( $e^+ - e^-$ ) pair annihilation, and marked differences in their contents in  $\gamma$ -ray line peaks due to the differences in the target compositions. Fig. 1 reports typical examples of experimental  $\gamma$ -ray energy spectra recorded in the single mode by an HP-Ge detector positioned at  $\theta_{\text{lab}} = 130^\circ$  for a 66 MeV proton beam interacting with the  $^{56}\text{Fe}$  target. As explained in Section 2, we further cleaned the recorded  $\gamma$ -ray energy spectra from the residual  $\gamma$ -ray Compton scattering background. Fig. 2 reports a net  $\gamma$ -ray energy spectrum from the same HP-Ge crystal corrected for the proton beam-induced background, the background from the reaction chamber, after additional suppression of the residual Compton scattering background in the subsequent phase of data analysis.

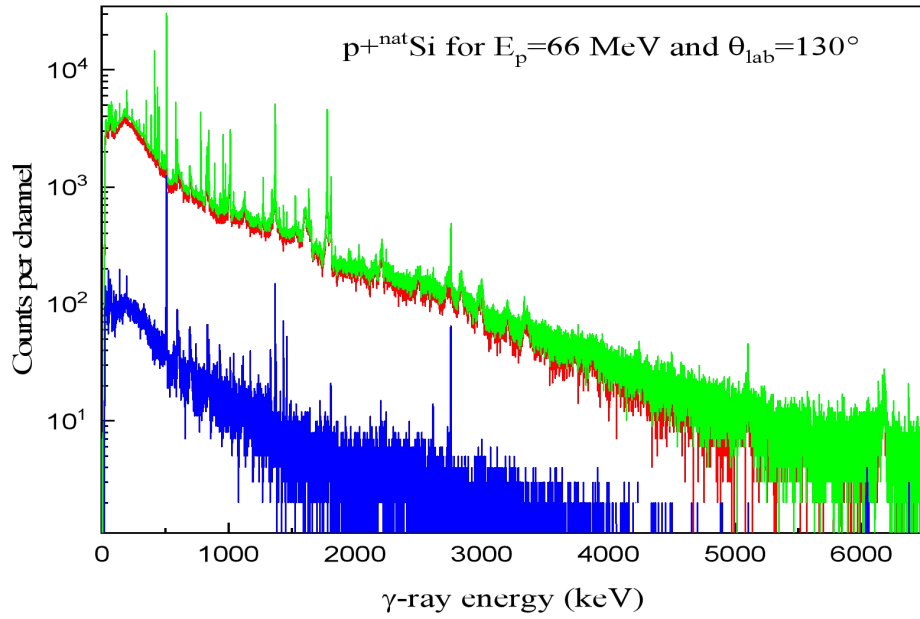


Fig. 1:  $\gamma$ -ray energy spectra recorded by an HP-Ge crystal positioned at  $\theta_{\text{lab}}=130^\circ$  in interaction of a 66 MeV proton beam with the  ${}^{\text{nat}}\text{Si}$  target. The total raw spectrum including the background with the target exposed to the proton beam is shown in green color. The background spectrum obtained with the proton beam passing through the empty-target frame (without target in place), normalized to the same accumulated beam charge, is depicted in blue, while the net spectrum obtained after background subtraction is depicted in red



materials. Besides the intense 511 keV line, other background line peaks are present in the  $\gamma$ -ray energy spectra, stemming from proton and secondary neutron-induced reactions on the surrounding Al and Ge elements constituting the reaction chamber, the target frames and holder and the HP-Ge crystals [48, 49]. They include the line transition at  $E_\gamma = 198$  keV arising from the  $^{70}\text{Ge} (n, \gamma)^{71\text{m}}\text{Ge}$  radiative neutron capture reaction, the line at  $E_\gamma = 595.85$  keV produced in the  $^{74}\text{Ge} (n, n'\gamma)^{74}\text{Ge}^*$  inelastic neutron scattering, and the lines at  $E_\gamma = 689.60$  and  $834.01$  keV originating from the  $^{72}\text{Ge} (n, n'\gamma)^{72}\text{Ge}^*$  inelastic neutron scattering. The  $\gamma$ -ray line at  $E_\gamma = 846.76$  keV from the  $^{56}\text{Fe} (p, p'\gamma)^{56}\text{Fe}$  inelastic proton scattering is also observed, together with the 843.76 keV line of  $^{27}\text{Al}$  produced both via the  $^{27}\text{Al} (p, p'\gamma)^{27}\text{Al}^*$  inelastic proton scattering and the  $\beta$ -decay of  $^{27}\text{Mg}$  following the  $^{27}\text{Al} (n, p)^{27}\text{Mg}^*$  charge-exchange reaction. The neutron-related  $\gamma$ -ray background line peaks were found to affect the measured  $\gamma$ -ray energy spectra from all the targets explored in our experiments (see Refs. [18, 36]).

The recorded  $\gamma$ -ray energy spectra from the  $^{\text{nat}}\text{Mg}$ ,  $^{\text{nat}}\text{Si}$  and  $^{56}\text{Fe}$  targets generally exhibited rather narrow and well separated lines of various intensities, less affected by Doppler effect (see Figs. (2, 3)) unlike the energy spectra taken from the Mylar and  $^{\text{nat}}\text{C}$  targets that contained strongly Doppler-shifted and broadened lines making their analysis more complex (see Ref. [36]). E.g., we mention here in passing the broad, strong, prominent in SFs  $\gamma$ -ray lines of  $^{12}\text{C}$  and  $^{16}\text{O}$  at  $E_\gamma$  4.439 and 6.129 MeV, corresponding respectively to the E2 ( $J^\pi = 2^+$ ,  $E_x = 4.439$  MeV,  $\tau = 42$  fs  $\rightarrow 0^+$ , g.s) and E3 ( $3^-$ , 6.129 MeV,  $\tau = 18.4$  ps  $\rightarrow 0^+$ , g.s) transitions. Produced mainly in  $(p, p')$  and  $(\alpha, \alpha')$  inelastic scatterings off the latter two targets and in reactions of accelerated  $^{12}\text{C}$  and  $^{16}\text{O}$  ions with abundant Hydrogen and Helium, they allow to extract precious information on the properties of the accelerated particle population, the underlying acceleration mechanisms and the magneto-hydrodynamic structure of the astrophysical sites [9 - 13], and require special line-shape analyses (see [36, 50] and references therein).

Table 2. Properties of the  $\gamma$ -ray transitions observed in proton-induced nuclear reactions on the  $^{nat}\text{Mg}$  target.

$E_\gamma$ (keV)	Intruder (keV)	Emitting nucleus	$E_i \rightarrow E_f$ (keV)	$J_i^\pi \rightarrow J_f^\pi$	Multipolarity	Branching ratio (%)
331.91		$^{21}\text{Na}$	331.9 $\rightarrow$ g.s	$5/2^+ \rightarrow 3/2^+$	M1+E2	100
350.73		$^{21}\text{Ne}$	350.73 $\rightarrow$ g.s	$5/2^+ \rightarrow 3/2^+$	M1+E2	100
389.71		$^{25}\text{Mg}$	974.76 $\rightarrow$ 585.05	$3/2^+ \rightarrow 1/2^+$	M1+E2	84.8
425.81		$^{24}\text{Al}$	425.8 $\rightarrow$ g.s	$1^+ \rightarrow 4^+$	M3	100
439.99		$^{23}\text{Na}$	439.99 $\rightarrow$ g.s	$5/2^+ \rightarrow 3/2^+$	M1+E2	100
450.7		$^{23}\text{Mg}$	450.71 $\rightarrow$ g.s	$5/2^+ \rightarrow 3/2^+$	M1+E2	100
472.2		$^{24}\text{Na}$	472.21 $\rightarrow$ g.s	$1^+ \rightarrow 4^+$	[M3]	100
563.19		$^{24}\text{Na}$	563.2 $\rightarrow$ g.s	$2^+ \rightarrow 4^+$	[E2]	3.74
585.03		$^{25}\text{Mg}$	585.05 $\rightarrow$ g.s	$1/2^+ \rightarrow 5/2^+$	E2	100
	583.04	$^{22}\text{Na}$	583.05 $\rightarrow$ g.s	$1^+ \rightarrow 3^+$	E2	100
937		$^{18}\text{F}$	937.2 $\rightarrow$ g.s	$3^+ \rightarrow 1^+$	E2	100
974.74		$^{25}\text{Mg}$	974.76 $\rightarrow$ g.s	$3/2^+ \rightarrow 5/2^+$	M1+E2	100
1016.9		$^{23}\text{Ne}$	1016.93 $\rightarrow$ g.s	$3/2^+ \rightarrow 5/2^+$	M1+E2	100
	1016.8	$^{22}\text{Na}$	2968.6 $\rightarrow$ 1951.5	$3^+ \rightarrow 2^+$	M1	100
1368.63		$^{24}\text{Mg}$	1368.67 $\rightarrow$ g.s	$2^+ \rightarrow 0^+$	E2	100
	1368.7	$^{22}\text{Na}$	1951.8 $\rightarrow$ 583.05	$2^+ \rightarrow 1^+$		100
1808.68		$^{26}\text{Mg}$	1808.74 $\rightarrow$ g.s	$2^+ \rightarrow 0^+$	E2	100
2754.02		$^{24}\text{Mg}$	4122.89 $\rightarrow$ 1368.67	$4^+ \rightarrow 2^+$	E2	100

Table 3. Same Table 2 but for the  $\gamma$ -ray transitions observed in proton-induced nuclear reactions on the  $^{nat}\text{Si}$  target.

$E_\gamma$ (keV)	Intruder (keV)	Emitting nucleus	$E_i \rightarrow E_f$ (keV)	$J_i^\pi \rightarrow J_f^\pi$	Multipolarity	Branching ratio (%)
331.91		$^{21}\text{Na}$	331.9 $\rightarrow$ g.s	$5/2^+ \rightarrow 3/2^+$	M1+E2	100
350.73		$^{21}\text{Ne}$	350.73 $\rightarrow$ g.s	$5/2^+ \rightarrow 3/2^+$	M1+E2	100
389.71		$^{25}\text{Mg}$	974.76 $\rightarrow$ 585.05	$3/2^+ \rightarrow 1/2^+$	M1+E2	84.8
416		$^{26}\text{Al}$	416.85 $\rightarrow$ g.s	$3^+ \rightarrow 5^+$	[E2]	100
439.99		$^{23}\text{Na}$	439.99 $\rightarrow$ g.s	$5/2^+ \rightarrow 3/2^+$	M1+E2	100
450.7		$^{23}\text{Mg}$	450.71 $\rightarrow$ g.s	$5/2^+ \rightarrow 3/2^+$	M1+E2	100
	451.7	$^{25}\text{Al}$	451.7 $\rightarrow$ g.s	$1/2^+ \rightarrow 5/2^+$	[E2]	100
585.03		$^{25}\text{Mg}$	585.05 $\rightarrow$ g.s	$1/2^+ \rightarrow 5/2^+$	E2	100
	583.04	$^{22}\text{Na}$	583.05 $\rightarrow$ g.s	$1^+ \rightarrow 3^+$	E2	100
780.8		$^{27}\text{Si}$	780.9 $\rightarrow$ g.s	$1/2^+ \rightarrow 5/2^+$	E2	100
843.46		$^{27}\text{Al}$	843.76 $\rightarrow$ g.s	$1/2^+ \rightarrow 5/2^+$	E2	100
	843.92	$^{26}\text{Al}$	2913.4 $\rightarrow$ 2069.47	$2^+ \rightarrow (2^+)$	[M1]	100
890.87		$^{22}\text{Na}$	890.89 $\rightarrow$ g.s	$4^+ \rightarrow 3^+$	M1+E2	100
957.3		$^{27}\text{Si}$	957.4 $\rightarrow$ g.s	$3/2^+ \rightarrow 5/2^+$	(M1+E2)	100
974.74		$^{25}\text{Mg}$	974.76 $\rightarrow$ g.s	$3/2^+ \rightarrow 5/2^+$	M1+E2	100
1273.36		$^{29}\text{Si}$	1016.93 $\rightarrow$ g.s	$3/2^+ \rightarrow 5/2^+$	M1+E2	100
1368.63		$^{24}\text{Mg}$	1368.67 $\rightarrow$ g.s	$2^+ \rightarrow 0^+$	E2	100
	1368.7	$^{22}\text{Na}$	1951.8 $\rightarrow$ 583.05	$2^+ \rightarrow 1^+$		100
1778.97		$^{28}\text{Si}$	1779.03 $\rightarrow$ g.s	$2^+ \rightarrow 0^+$	E2	100

Table 4. Same Table 2 but for the  $\gamma$ -ray transitions observed in proton-induced nuclear reactions on the  $^{56}\text{Fe}$  target.

$E_\gamma$ (keV)	Intruder (keV)	Emitting nucleus	$E_i \rightarrow E_f$ (keV)	$J_i^\pi \rightarrow J_f^\pi$	Multipolarity	Branching ratio (%)
125.95		$^{55}\text{Mn}$	125.95 $\rightarrow$ g.s	$7/2^- \rightarrow 5/2^-$	M1+(E2)	100
156.29		$^{54}\text{Mn}$	156.27 $\rightarrow$ g.s	$4^+ \rightarrow 3^+$	M1+E2	100
211.98		$^{54}\text{Mn}$	368.22 $\rightarrow$ 165.29	$5^+ \rightarrow 4^+$	M1	100
226.3		$^{50}\text{V}$	226.21 $\rightarrow$ g.s	$5^+ \rightarrow 6^+$	M1+(E2)	100
	226.43	$^{54}\text{Mn}$	4998.1 $\rightarrow$ 4771.6	$(15)^+ \rightarrow 10^+$	(M1)	100
274.8		$^{55}\text{Fe}$	2813.8 $\rightarrow$ 2539.11	$13/2^- \rightarrow 11/2^+$	M1+(E2)	100
377.88		$^{53}\text{Mn}$	377.89 $\rightarrow$ g.s	$5/2^- \rightarrow 7/2^-$	M1+E2	100
411.9		$^{55}\text{Fe}$	411.42 $\rightarrow$ g.s	$1/2^- \rightarrow 3/2^-$	M1+(E2)	100
	411.4	$^{54}\text{Fe}$	2949.2 $\rightarrow$ 2538.1	$6^+ \rightarrow 4^+$	E2	100
783.3		$^{50}\text{Cr}$	783.31 $\rightarrow$ g.s	$2^+ \rightarrow 0^+$	E2	100
846.77		$^{56}\text{Fe}$	846.77 $\rightarrow$ g.s	$2^+ \rightarrow 0^+$	E2	100
	847	$^{55}\text{Fe}$	2255.5 $\rightarrow$ 1408.45	$\rightarrow 7/2^-$		100
931.29		$^{55}\text{Fe}$	931.29 $\rightarrow$ g.s	$5/2^- \rightarrow 3/2^-$	M1+E2	100
	931.2	$^{54}\text{Mn}$	2515.2 $\rightarrow$ 1784.04	$5^+ \rightarrow 7^+$		100
	931.04	$^{54}\text{Mn}$	2856.55 $\rightarrow$ 1925.35	$8^+ \rightarrow 7^-$	M1	46.4
935.53		$^{52}\text{Cr}$	2369.63 $\rightarrow$ 1434.091	$4^+ \rightarrow 2^+$	E2	100
	936.9	$^{54}\text{Fe}$	6864.3 $\rightarrow$ 5927.4	$8^+ \rightarrow 7^+$	M1+(E2)	100
1098.1		$^{50}\text{Cr}$	1881.42 $\rightarrow$ 783.41	$4^+ \rightarrow 2^+$	E2	100
1121.7		$^{53}\text{Mn}$	2562.99 $\rightarrow$ 1441.15	$13/2^+ \rightarrow 11/2^-$	M1+(E2)	100
1129.9		$^{54}\text{Fe}$	2538.1 $\rightarrow$ 1408.19	$4^+ \rightarrow 2^+$	E2	100
1122.5		$^{55}\text{Fe}$	2539.11 $\rightarrow$ 1316.54	$7/2^- \rightarrow 11/2^-$	E2	100
1238.27		$^{56}\text{Fe}$	2085.1 $\rightarrow$ 846.78	$4^+ \rightarrow 2^+$	E2	100
1253.7		$^{52}\text{Mn}$	1253.7 $\rightarrow$ g.s	$5^+ \rightarrow 6^+$		100
	1251.1	$^{51}\text{Mn}$	1488.5 $\rightarrow$ 237.3	$11/2^- \rightarrow 7/2^-$	E2	100
	1252.1	$^{53}\text{Mn}$	2693.29 $\rightarrow$ 1441.15	$15/2^- \rightarrow 11/2^-$	E2	100
1282.5		$^{50}\text{Cr}$	3164.06 $\rightarrow$ 1881.42	$6^+ \rightarrow 4^+$	E2	100
1289.83		$^{53}\text{Mn}$	1289.83 $\rightarrow$ g.s	$3/2^- \rightarrow 7/2^-$	E2	100
	1289.59	$^{53}\text{Cr}$	1289.59 $\rightarrow$ g.s	$7/2^- \rightarrow 3/2^-$	E2	100
1303.4		$^{56}\text{Fe}$	3388.55 $\rightarrow$ 2085.1	$6^+ \rightarrow 4^+$	E2	100
1316.4		$^{55}\text{Fe}$	1316.54 $\rightarrow$ g.s	$7/2^- \rightarrow 3/2^-$	E2	100
	1312.6	$^{56}\text{Fe}$	4683.04 $\rightarrow$ 3369.95	$2^+, (3^+) \rightarrow 2^+$	E2	<48
1328.2		$^{53}\text{Fe}$	1328.01 $\rightarrow$ g.s	$9/2^- \rightarrow 7/2^-$	M1+(E2)	100
	1328.95	$^{52}\text{Fe}$	5654.5 $\rightarrow$ 4325.5	$6^+ \rightarrow 6^+$	(E2)	100
1333.65		$^{52}\text{Cr}$	2767.77 $\rightarrow$ 1434.1	$4^+ \rightarrow 2^+$	E2	100
1369.7		$^{55}\text{Fe}$	2301.06 $\rightarrow$ 931.29	$(9/2^-) \rightarrow 5/2^-$	(E2)	100
1408.4		$^{55}\text{Fe}$	1408.45 $\rightarrow$ g.s	$7/2^- \rightarrow 3/2^-$	E2	84
	1408.1	$^{54}\text{Fe}$	1408.19 $\rightarrow$ g.s	$2^+ \rightarrow 0^+$	E2	100
1434.07		$^{52}\text{Cr}$	1434.09 $\rightarrow$ g.s	$2^+ \rightarrow 0^+$	E2	100
1441.2		$^{53}\text{Mn}$	1441.15 $\rightarrow$ g.s	$11/2^- \rightarrow 7/2^-$	E2	100
1480.3		$^{51}\text{Cr}$	1480.07 $\rightarrow$ g.s	$11/2^- \rightarrow 7/2^-$	E2	100
1810.76		$^{56}\text{Fe}$	2657.59 $\rightarrow$ 846.78	$2^+ \rightarrow 2^+$	M1+E2	100
2273.2		$^{56}\text{Fe}$	3120.11 $\rightarrow$ 846.78	$(1)^+ \rightarrow 2^+$		100
	2273.1	$^{54}\text{Mn}$	2398.4 $\rightarrow$ 125.94	$9/2^- \rightarrow 7/2^-$		100

#### 4.2 $\gamma$ -ray absolute detection efficiencies

Fig. 3 reports, as a typical example, the variation of the absolute detection efficiency,  $\varepsilon(E_\gamma, \theta)$ , versus the photon energy for a single HP-Ge crystal set at  $\theta_{lab} = 130^\circ$ . It shows the experimental efficiency data taken by the standard radioactive sources, the GEANT4-

simulated values normalized to the latter data set and the fitted curve to both two data sets generated by the multiparametric function of Eq. 2. The fit curves to the efficiency data were finally used for calculating the efficiencies for all the 32 HP-Ge detectors and all the explored targets. Other results for the absolute detection efficiencies have been reported and discussed in details in our previous papers with accounting for their proton energy dependence (see Refs. [18, 36]).

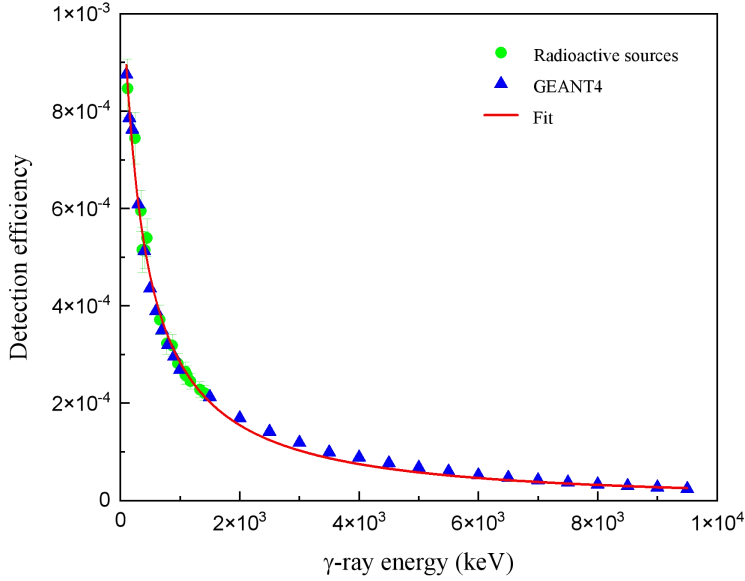
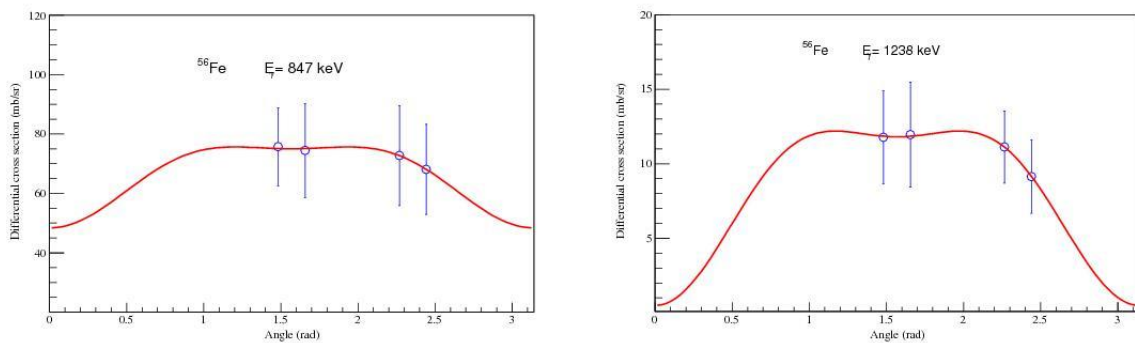


Fig. 3: absolute  $\gamma$ -ray detection efficiencies for a single HP-Ge crystal located at  $\theta_{lab} = 130^\circ$ . The green circles represent the absolute efficiency data measured with the calibrated radioactive sources of  $^{152}\text{Eu}$ ,  $^{60}\text{Co}$  and  $^{137}\text{Cs}$ . The blue triangles correspond to the normalized GEANT4-simulated values, while the fitted curve to these two data sets is shown by the red solid line.

In order to evaluate the uncertainties associated with the efficiency determination, we primarily considered the statistical uncertainty arising from the calculation of the areas under the full-energy absorption peaks. This statistical uncertainty was added in quadrature to the uncertainty in the activity of the radioactive sources and the uncertainty associated with the branching ratios. The uncertainty in the detection efficiency data taken by the radioactive sources was dominated by that affecting the radioactive source activities amounting to 4 – 5%, the branching ratios contributed by less than 1%, while the statistical uncertainty in the  $\gamma$ -ray line peak areas amounted to 1-2%. Thus, an average value of the overall uncertainty in (E) from the radioactive sources of approximately 7% was obtained. Upon adding in quadrature the uncertainties associated with the GEANT4-simulated efficiency values, the normalization factors, and the fits of the multi-parametric function to the data, the total uncertainty in (E) increased to  $\sim 12\%$ .

### 4.3 $\gamma$ -ray Angular distributions

The experimental  $\gamma$ -ray differential cross sections from the 32 HP-Ge detectors produced mainly in (p, p' $\gamma$ ) inelastic proton scattering were found to be dominated by E2 and (M1 + E2) transitions. They were averaged for each observation angle  $\theta$  relative to the incident proton beam direction and versus the  $\gamma$ -ray line energy, assuming  $\theta_{lab} \approx \theta_{c.m.}$ . As illustrative examples, we report in Fig. 4 the corresponding experimental data points versus the proton beam energy for some prominent  $\gamma$ -ray lines produced in proton-induced nuclear reactions on the  $^{nat}\text{Mg}$ ,  $^{nat}\text{Si}$  and  $^{56}\text{Fe}$  targets at  $E_p = 66$  and 125 MeV, together with the associated best-fit curves generated by Eq. (4). Tables 5-7 display the associated  $a_\ell$  fit coefficients of the least-squares Legendre polynomial expansion. The reduced  $\chi^2$ -values resulting from the fits amounted to at most 1 for the narrow, isolated  $\gamma$ -ray lines, and to at most 3 in case of overlapping, broader line structures within the  $\gamma$ -ray energy spectra. We derived the total relative uncertainties in the experimental differential cross sections (also shown in Fig. 4) for all the analyzed  $\gamma$ -ray transitions by adding in quadrature the uncertainties in the quantities entering Eq. (2), i.e., the contributions from the photopeak area determination, the absolute detection efficiency, the target thickness amounting to 3%, and the collected beam charge (1%). These uncertainties were combined in quadrature to obtain the total relative uncertainty for each HP-Ge crystal. The uncertainties in the mean differential cross section values at each observation angle were defined as the absolute differences between the maximum values and the mean values. Finally, an overall, average, total relative uncertainty of 19 % was obtained. Alternatively, the total relative uncertainties in the experimental angular distributions were estimated by adding in quadrature the uncertainties affecting the parameters of the Legendre polynomial expansion in Eq. (4), leading to consistent values lying within the range of 18-20%.



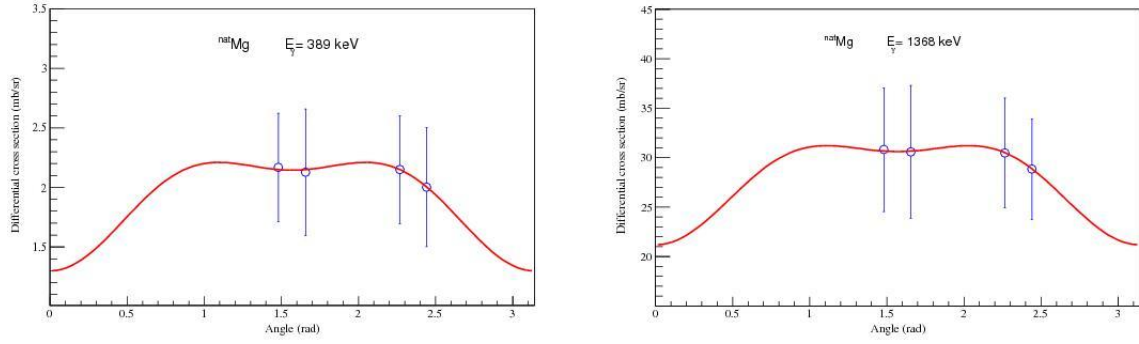


Fig. 4. Illustrative examples of  $\gamma$ -ray experimental angular distributions for proton-induced nuclear reactions on the  $^{nat}\text{Mg}$ ,  $^{nat}\text{Si}$  and  $^{56}\text{Fe}$  targets (blue symbols) and corresponding Legendre polynomial expansion fits (red curves): (a) for proton energy  $E_p = 66$  MeV, (b) for  $E_p = 125$  MeV.

Table 5. List of the Legendre polynomial coefficients  $a_l$  obtained by fitting the  $\gamma$ -ray angular distributions with Eq. (3) on the  $^{nat}\text{Mg}$  target.

$\gamma$ -ray energy (keV)	$E_p = 66$ MeV			$E_p = 80$ MeV			$E_p = 95$ MeV			$E_p = 110$ MeV			$E_p = 125$ MeV		
	$a_0$	$a_2$	$a_4$	$a_0$	$a_2$	$a_4$	$a_0$	$a_2$	$a_4$	$a_0$	$a_2$	$a_4$	$a_0$	$a_2$	$a_4$
	<b>p + <math>^{nat}\text{Mg}</math></b>														
<b>331.91</b>	7.13	0.40	0.35	6.88	0.10	-0.17	6.64	-0.19	-0.70	6.08	-0.70	-2.59	5.03	-1.55	-2.25
<b>350.73</b>	23.23	-1.13	0.83	21.78	-2.97	-1.17	20.33	-4.81	-3.17	18.44	-5.47	-4.04	16.96	-0.15	-0.77
<b>389.71</b>	2.06	-0.43	-0.34	1.77	-0.40	-0.29	1.49	-0.36	-0.25	1.31	-0.21	-0.11	1.19	-0.25	-0.17
<b>425.81</b>	0.92	-0.27		0.71	-0.21		0.51	-0.14		0.36	-0.16		0.30	0.0	
<b>439.99</b>	35.55	-4.05	-2.57	33.39	-4.66	-4.02	31.22	-5.28	-5.46	29.39	-2.21	-2.31	27.15	13.59	1.73
<b>450.7</b>	37.01	-5.15	-3.90	35.89	-5.58	-4.89	34.77	-6.00	-5.88	31.24	-6.08	-5.61	27.69	1.74	-1.43
<b>472.2</b>	4.06	-0.22		3.63	-0.06		3.21	0.11		3.20	0.05		2.73	-0.39	
<b>585.03</b>	34.22	-7.70	-7.95	31.42	-5.77	-6.59	28.62	-3.84	-5.23	26.04	-6.63	-6.57	23.38	-0.34	-7.99
<b>930.7</b>	2.66	5.92	4.85	2.27	2.94	2.46	1.55	2.79	1.84	0.83	0.41	0.68	0.58	0.25	0.79
<b>937</b>	7.36	1.77	1.08	7.02	0.54	0.13	6.68	-0.69	-0.81	6.46	0.04	0.32	5.92	-0.07	-1.10
<b>974.74</b>	2.20	-0.51	-0.08	1.79	-0.21	0.02	1.39	0.10	0.11	1.28	0.21	0.22	1.04	0.09	0.01
<b>1016.9</b>	2.77	0.37	0.88	2.44	-0.15	0.22	2.11	-0.67	-0.45	2.05	-0.68	-0.68	1.66	-0.72	-0.48
<b>1368.63</b>	56.53	-2.96	-1.68	49.22	-2.93	-0.57	41.90	-2.90	0.54	34.60	-1.59	0.55	29.53	-4.83	-3.60
<b>1808.68</b>	5.28	-0.31	0.36	4.57	-1.33	0.13	3.86	-2.35	-0.10	3.42	-0.05	0.63	2.76	-1.44	0.27
<b>2754.02</b>	12.05	4.85	8.25	11.09	1.28	5.23	10.12	-2.30	2.20	9.66	1.89	5.25	9.44	1.82	3.26

Table 6. Same as in Table 5 but for the  $^{nat}\text{Si}$  target.

$\gamma$ -ray energy (keV)	$E_p = 66 \text{ MeV}$			$E_p = 80 \text{ MeV}$			$E_p = 95 \text{ MeV}$			$E_p = 110 \text{ MeV}$			$E_p = 125 \text{ MeV}$		
	a <sub>0</sub>	a <sub>2</sub>	a <sub>4</sub>	a <sub>0</sub>	a <sub>2</sub>	a <sub>4</sub>	a <sub>0</sub>	a <sub>2</sub>	a <sub>4</sub>	a <sub>0</sub>	a <sub>2</sub>	a <sub>4</sub>	a <sub>0</sub>	a <sub>2</sub>	a <sub>4</sub>
	<b>p + <math>^{nat}\text{Si}</math></b>														
<b>331.91</b>	1.29	-0.20	0.01	1.99	-0.02	-0.39	2.13	-1.26	-1.02	2.32	-0.22	-0.11	2.19	-0.55	-0.28
<b>350.73</b>	6.59	-1.35	-0.78	9.96	-2.43	-3.19	10.98	-2.58	-3.19	10.21	-2.64	-2.37	10.59	-3.16	-3.36
<b>389.71</b>	5.08	0.05	-0.52	4.86	-1.24	-1.46	4.49	-1.19	-1.32	3.70	-0.80	-1.84	3.58	-1.61	-1.83
<b>416</b>	30.54	-6.97	-7.35	29.28	-3.61	-5.67	25.03	-6.01	-10.18	22.42	-5.95	-7.52	19.58	-3.68	-7.10
<b>439.99</b>	16.86	-4.85	-4.86	13.64	-7.02	-8.16	15.14	-5.31	-3.91	13.77	-5.48	-5.85	13.90	-4.52	4.76
<b>450.7</b>	10.32	-2.87	-3.83	8.71	-2.50	-4.59	8.36	-3.03	-4.29	7.69	-3.46	-3.91	6.42	-2.17	-4.04
<b>585.03</b>	21.14	-3.50	-2.85	21.37	-2.04	-2.79	20.64	-3.89	-4.03	18.77	0.45	-2.64	18.44	-0.20	-0.58
<b>780.8</b>	14.57	-3.31	-3.23	13.88	-4.75	-6.03	13.81	-2.26	-2.35	9.25	-2.66	-2.68	10.92	-0.72	-0.75
<b>843.76</b>	10.01	-1.95	-1.57	9.12	-3.62	-3.24	8.82	-1.89	-1.45	7.51	-3.58	-3.95	7.02	-2.64	-3.09
<b>890.87</b>	3.81	-0.22	-0.37	3.58	-1.18	-1.56	3.54	-0.43	-0.21	3.87	-1.13	-1.05	3.41	-3.60	-3.02
<b>957.3</b>	13.00	-0.77	-1.09	12.25	-1.45	-2.00	11.30	-1.60	-1.77	11.08	-3.18	-3.25	8.86	-0.65	-0.68
<b>974.74</b>	4.82	-0.65	-0.37	5.00	0.09	-0.19	4.66	-1.29	-1.27	4.30	-0.85	-0.52	3.78	-1.36	-1.30
<b>1273.36</b>	7.83	-1.98	-1.61	7.21	-2.03	-2.63	6.92	-0.46	-0.72	6.69	-0.19	-0.33	6.57	-0.94	-0.50
<b>1368.63</b>	44.03	-0.41	0.54	48.09	-0.08	0.42	45.59	-4.52	-1.65	41.94	-5.44	-1.44	43.58	6.19	5.45
<b>1778.97</b>	61.85	-8.64	-7.05	52.81	-5.06	-1.48	43.70	-5.76	-3.02	34.86	-0.756	1.52	30.08	-1.66	2.84

Table 7. Same as in Table 5 but for the  $^{56}\text{Fe}$  target.

$\gamma$ -ray energy (keV)	$E_p = 66 \text{ MeV}$			$E_p = 80 \text{ MeV}$			$E_p = 95 \text{ MeV}$			$E_p = 110 \text{ MeV}$			$E_p = 125 \text{ MeV}$		
	a <sub>0</sub>	a <sub>2</sub>	a <sub>4</sub>	a <sub>0</sub>	a <sub>2</sub>	a <sub>4</sub>	a <sub>0</sub>	a <sub>2</sub>	a <sub>4</sub>	a <sub>0</sub>	a <sub>2</sub>	a <sub>4</sub>	a <sub>0</sub>	a <sub>2</sub>	a <sub>4</sub>
	<b>p + <math>^{56}\text{Fe}</math></b>														
<b>126.95</b>	12.46	0.08	0.67	13.62	-3.79	-1.76	12.83	-1.33	0.44	11.87	-0.54	1.49	9.15	5.43	4.11
<b>156.29</b>	54.10	-8.49	0.85	52.89	-5.84	4.88	45.92	-7.12	-0.51	41.31	-7.45	-2.55	33.66	8.25	7.65
<b>211.98</b>	28.89	-2.55		28	-3.3		23.81	-2.33		19.7	-0.94		16.16	-0.77	
<b>226.43</b>	10.93	-0.51		9.96	-0.43		10.49	-0.33		11.14	-0.26		8.40	-1.06	
<b>274.8</b>	8.99	-1.73	-1.54	13.54	-1.61	0.36	10.76	-1.31	-0.27	8.72	-2.67	-1.28	7.40	1.83	1.11
<b>377.88</b>	35.45	-11.86	-9.62	33.75	-9.07	-7.94	28.77	-8.90	-7.22	25.13	-7.31	-5.83	22.87	-6.65	-5.30
<b>411.9</b>	31.72	-5.10	-8.19	29.61	-7.72	-9.12	24.68	-9.82	-6.81	21.02	-2.50	-1.63	17.96	-2.14	-1.39
<b>783.3</b>	33.4	-5.73	-7.65	25.72	-5.24	-5.46	26.62	-5.19	-7.72	29.06	-1.49	-1.71	20.82	-2.08	-3.09
<b>846.77</b>	70.90	-14.43	-8.32	64.68	-11.01	-7.47	49.33	-18.3	-11.81	38.72	-12.82	-8.02	29.82	2.64	0.83
<b>931.29</b>	44.68	-3.46	-4.04	41.4	-6.28	-12.47	33.85	-20.34	-14.88	28.39	-9.60	-7.86	22.19	-8.62	-9.58
<b>935.53</b>	18.36	0.82	-4.19	23.32	1.90	-1.76	18.95	-3.91	-7.44	16.56	-2.89	-4.77	14.57	-11.04	-13.33
<b>1098.1</b>	23.71	-2.81	-2.81	17.52	-1.07	-1.00	19.16	-2.49	-2.21	20.64	-2.28	-1.26	15.78	3.39	4.37
<b>1121.7</b>	11.66	-4.87	-3.18	12.98	-4.23	-2.84	11.61	-1.10	-0.68	10.47	-1.38	-1.73	10.42	-4.28	-9.17
<b>1129.9</b>	38.55	-1.37	-1.53	34.22	-2.75	-0.53	27.38	-2.61	-1.28	22.08	-2.08	-0.31	22.22	-6.81	-7.15
<b>1222.5</b>	14.69	0.26	0.31	13.28	-2.56	-0.70	11	-2.57	-1.15	9.42	-1.18	0.12	8.48	-0.73	-0.17
<b>1238.27</b>	20.39	-4.70	-3.42	19.08	-3.38	-0.17	15.51	-4.27	-1.55	11.89	-4.11	-2.72	10.21	-6.02	-3.79
<b>1252.1</b>	16.65	2.53	-1.13	13.11	-2.82	-3.23	11.63	-0.70	-1.03	9.62	-0.33	-0.26	7.51	2.5	0.73
<b>1282.5</b>	12.40	-1.92	-2.64	9.55	0.48	0.54	9.93	-1.59	-1.64	12.26	-2.36	-1.84	9.98	3.36	3.15
<b>1289.83</b>	11.11	0.51	1.65	11.78	0.23	0.73	10.21	-2.85	-1.97	9.11	-2.37	-1.09	8.14	-2.11	-0.97
<b>1303.4</b>	3.48	0.91	0.54	3.56	1.72	2.23	2.53	-0.71	-0.51	2.14	-1.28	-0.72	1.93	-6.04	-5.29
<b>1316.04</b>	38.27	2.67	1.39	35.41	-5.07	-2.42	32.49	-3.75	-2.74	27.55	-3.73	-2.16	21.00	5.76	6.93
<b>1328.2</b>	3.04	-1.83	-1.64	2.70	-3.44	-3.97	2.30	-1.59	-1.76	2.17	0.01	0.81	1.96	1.97	3.41
<b>1333.65</b>	11.51	-4.37	-2.71	15.35	-0.57	-0.14	13.13	0.67	1.08	11.72	0.27	1.35	10.46	0.24	1.20
<b>1369.7</b>	7.05	2.59	2.95	6.49	-2.64	-1.42	5.47	-0.33	-1.67	4.80	3.64	1.60			
<b>1408.4</b>	87.04	-14.92	-16.15	84.34	-5.92	-0.33	72.29	0.78	5.11	57.82	-2.79	0.12	45.56	4.28	7.67
<b>1434.07</b>	54.21	-8.47	-7.74	64.29	-4.15	-5.68	60.36	-1.93	0.36	51.69	-6.18	-3.38	42.71	8.31	12.53
<b>1441.2</b>	47.79	3.38	-0.20	36.53	0.62	-1.46	30.17	0.04	2.21	25.04	-1.21	3.31	18.2	5.67	7.69
<b>1480.3</b>	4.01	-0.89	-1.05	7.19	-2.54	-1.95	9.28	0.58	1.24	7.81	0.08	0.10	5.89	1.86	2.28
<b>1810.76</b>	8.81	2.74	4.04	7.01	-0.04	2.16	6.57	-3.55	0.84	5.17	-2.59	-1.43	4.85	-3.32	-0.76
<b>2273.2</b>	1.79	-1.09	-0.88	1.47	-2.19	2.18	1.15	-1.55	-0.86	0.93	-0.35	-0.49	0.77	-0.43	-0.70

#### 4.4 Total $\gamma$ -ray line production cross sections

As stated, we have determined the total  $\gamma$ -ray line production cross sections in terms of the  $a_0$  coefficients of the Legendre polynomial expansion of Eq. (4) fitted to the differential cross section experimental data. This can be done by the relation  $\sigma = 4\pi a_0$ , provided one uses the intrinsic detection efficiencies in Eq. (3). However, since the differential cross sections were calculated using instead the absolute detection efficiencies, we derived the total cross sections simply as  $\sigma = a_0$ .

To ensure the homogeneity and consistency of the cross sections derived from different experimental runs, particularly those performed with targets of different isotopic compositions, we normalized the cross section experimental data sets from Refs. [17, 24, 25, 29] involving the  $^{nat}\text{Fe}$  target to the isotopic composition of  $^{56}\text{Fe}$ . Similarly, the cross section data sets from Refs. [20, 24, 25] taken with the  $^{24}\text{Mg}$  target were adjusted to the natural isotopic abundance of magnesium.

The obtained  $\sigma(E_p)$  experimental results are reported in Figs. (5-12) for the analyzed  $\gamma$ -ray lines, where they are compared to previous experimental data sets from the literature when available. They concern a total of sixty  $\gamma$ -ray lines produced in nuclear reactions induced by 66, 80, 100, 110 and 120 MeV proton beams on the  $^{nat}\text{Mg}$ ,  $^{nat}\text{Si}$  and  $^{56}\text{Fe}$  targets. More precisely, Figs (5, 6) report the  $\sigma(E_p)$  results for 15 lines observed in proton irradiation of the  $^{nat}\text{Mg}$  target, Figs. (7, 8) report similar results for 15 lines from the  $^{nat}\text{Si}$  target, and Figs. (9-12) report the results for 30  $\gamma$ -ray lines from the  $^{56}\text{Fe}$  target. The numerical values of the total  $\gamma$ -ray line production cross sections from these three targets are respectively listed in Tables (8, 9, 10) along with the corresponding average relative uncertainties. The uncertainties in the differential cross sections affect the Legendre polynomial expansion fits to the experimental data and influence the extracted values of the  $a$  coefficients and their associated uncertainties. This effect is particularly significant for the zero-order term,  $a_0$ , used for calculating the total  $\gamma$ -ray line cross sections and the associated relative uncertainties, found to amount to 12-19%.

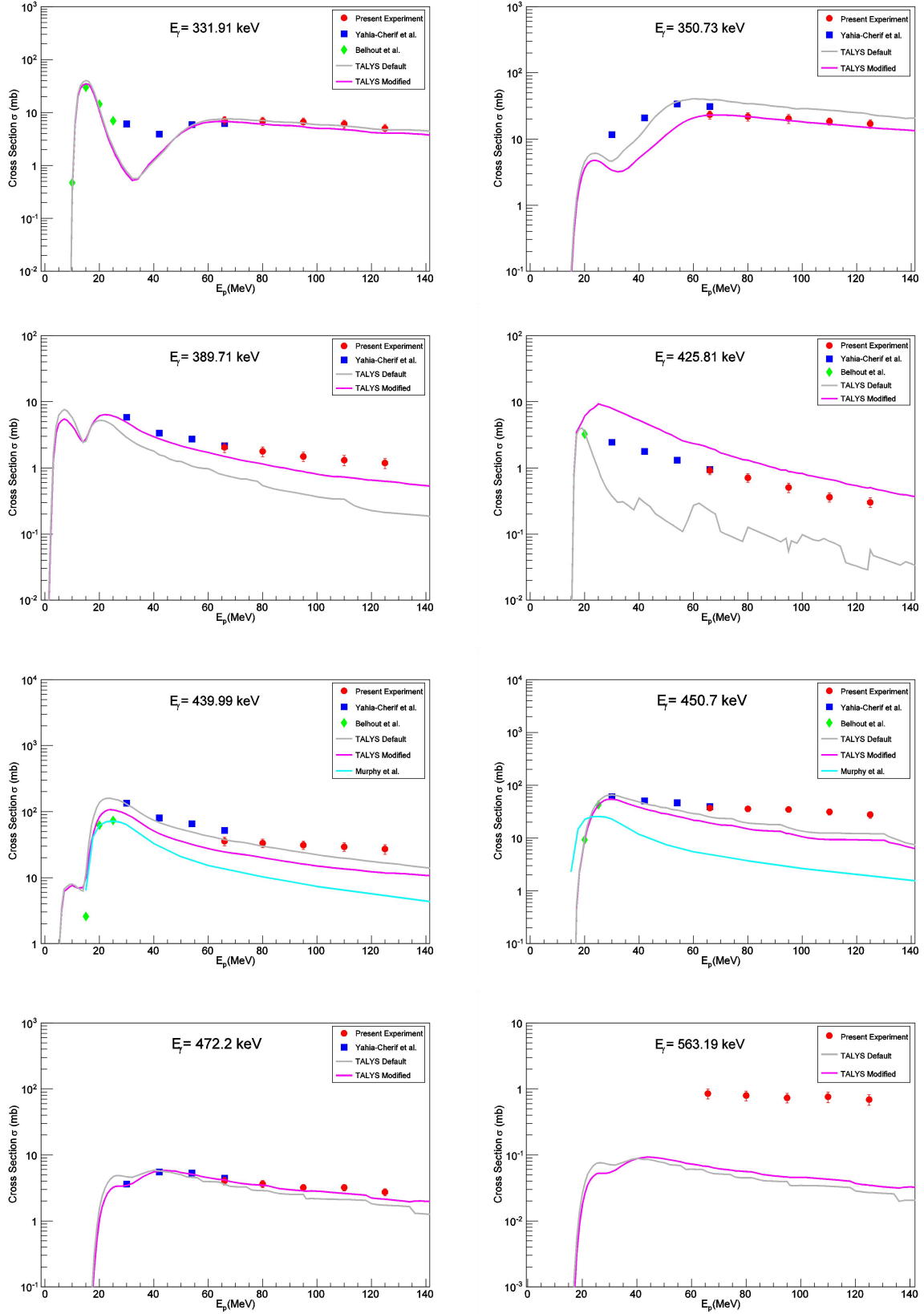


Fig. 5. Total production cross sections for 8  $\gamma$ -ray lines produced in proton reactions with the  $^{nat}\text{Mg}$  target. The experimental data are shown as follows: in red full circles (data from this work), in blue full squares (data of Yahia-Cherif et al. [18]), in green full diamonds (data of Belhout et al. [24, 25]), in black, down-oriented full triangles (data of Dyer et al. [20]), and in yellow, up-oriented full triangles (Lesko et al. [29] data). The Teal curves correspond to the predictions of the Murphy et al. semi-empirical compilation [31]. The grey curves represent the results derived by TALYS code [32] calculations with default input parameters, while the pink curves refer to TALYS code calculations using our modified OMPs and  $\beta_\lambda$  level deformation parameters.

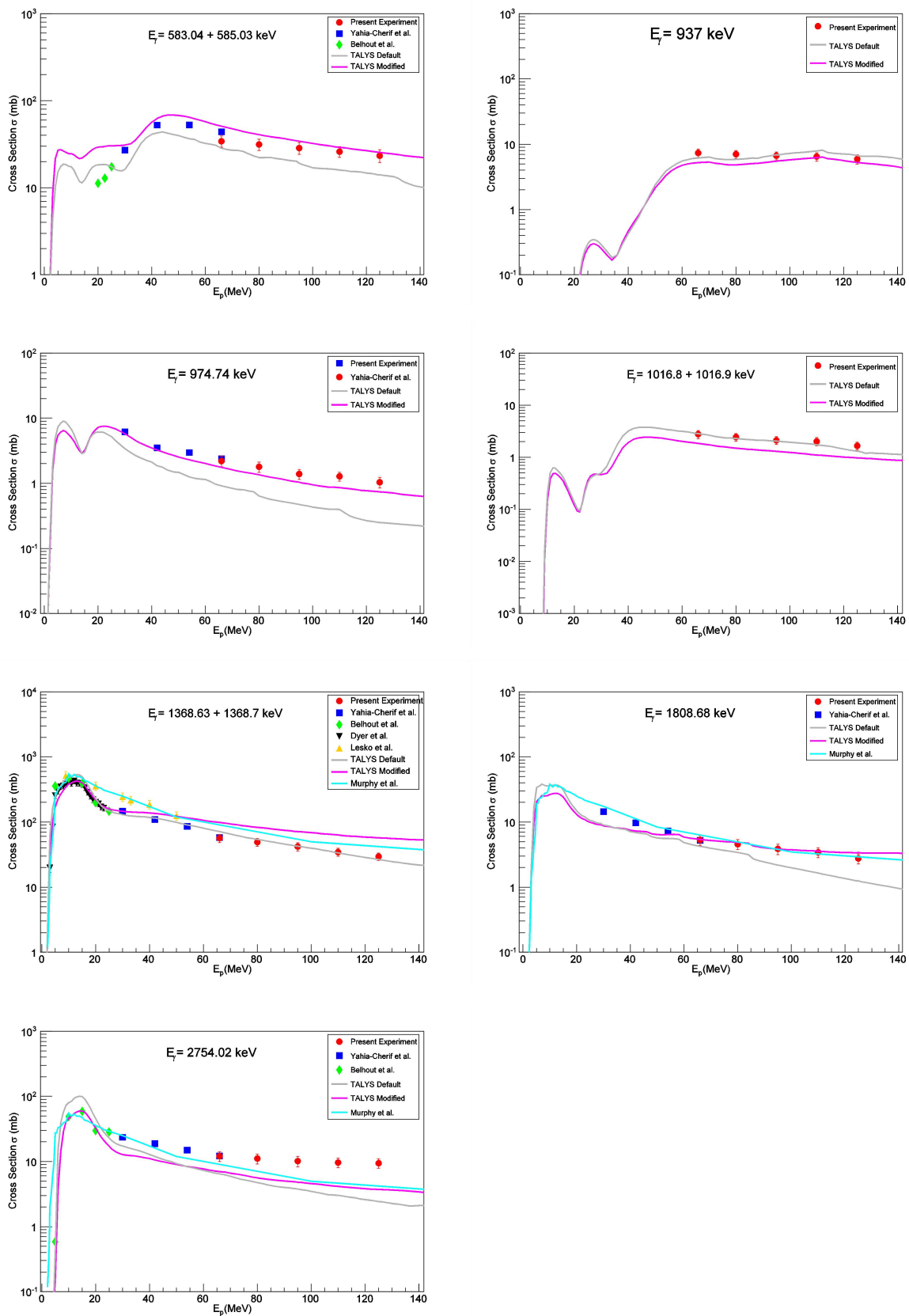


Fig. 6. Same as in Fig.5 but for 7 other  $\gamma$ -ray lines emitted in proton interactions with the  $^{nat}\text{Mg}$  target.

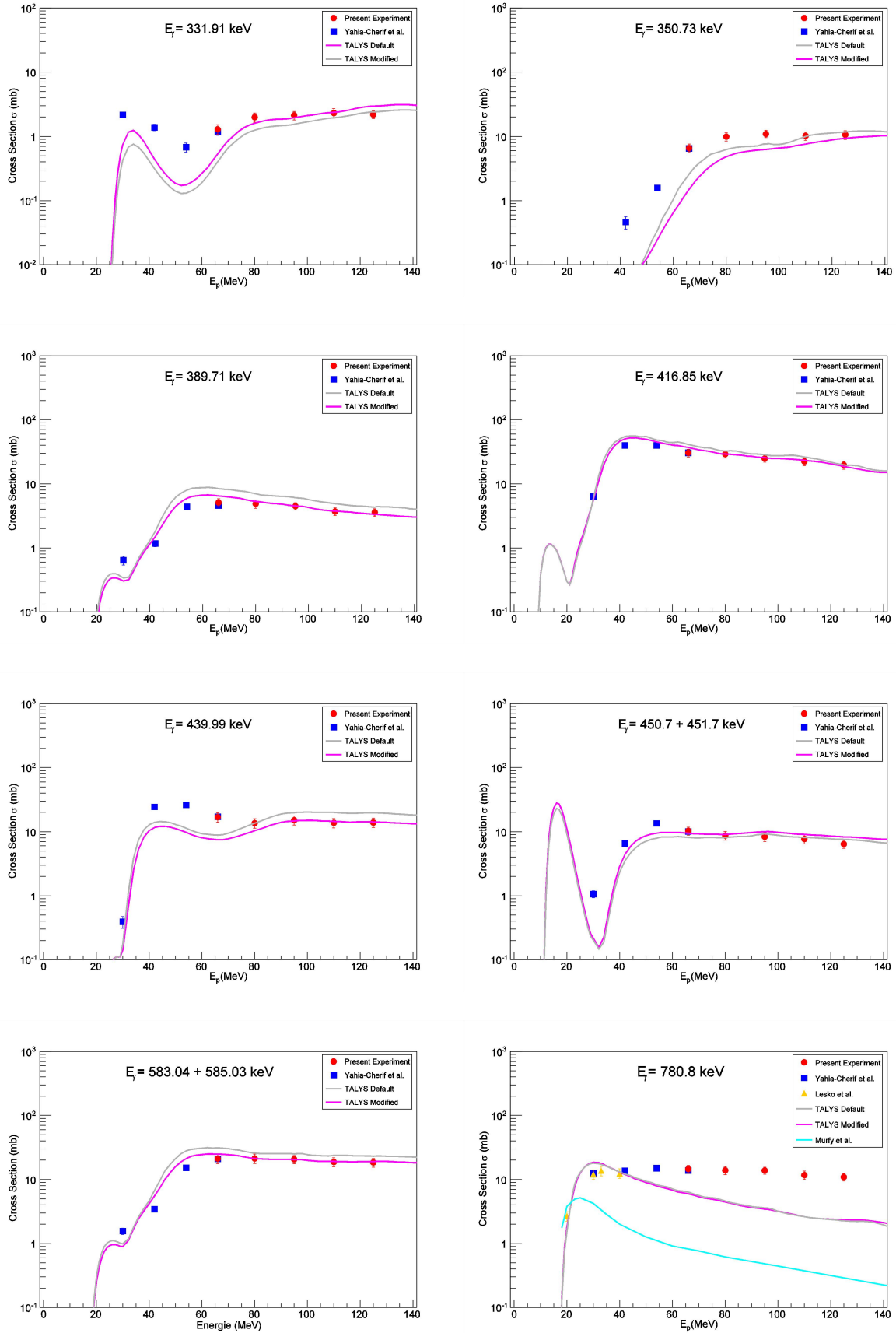


Fig. 7. Same as in Fig. 5 but for 8  $\gamma$ -ray lines produced in proton reactions with the  $^{nat}\text{Si}$  target.

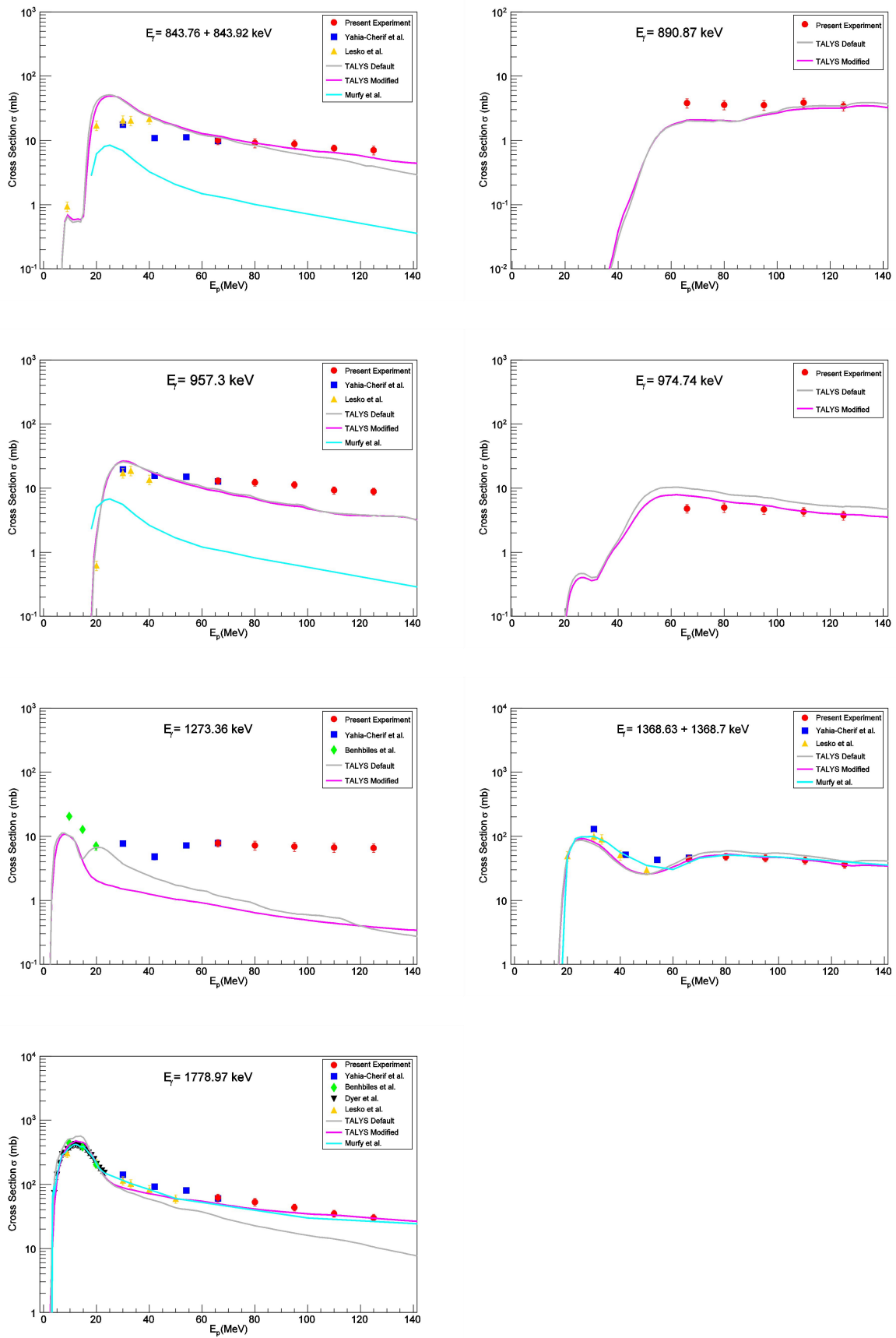


Fig. 8. Same as in Figs. 5 but for seven 7 other  $\gamma$ -ray lines produced in proton reactions with the  $^{nat}\text{Si}$  target. The same symbols are used, except that here the green circles represent the experimental data of Benhabiles et al. [17].

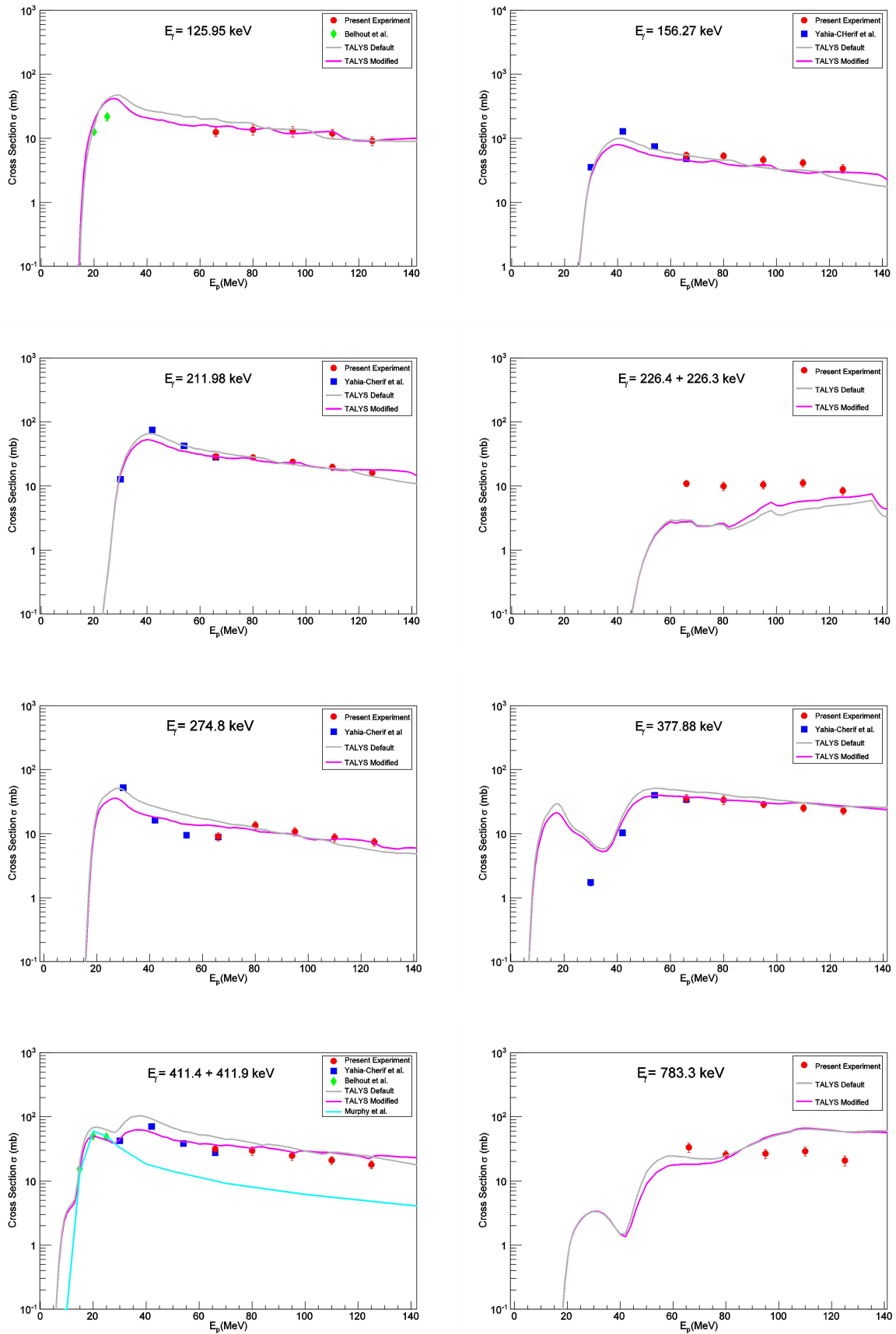


Fig. 9. Same as in Fig. 5 but for 8  $\gamma$ -ray lines produced in proton reactions with the  $^{56}\text{Fe}$  target.

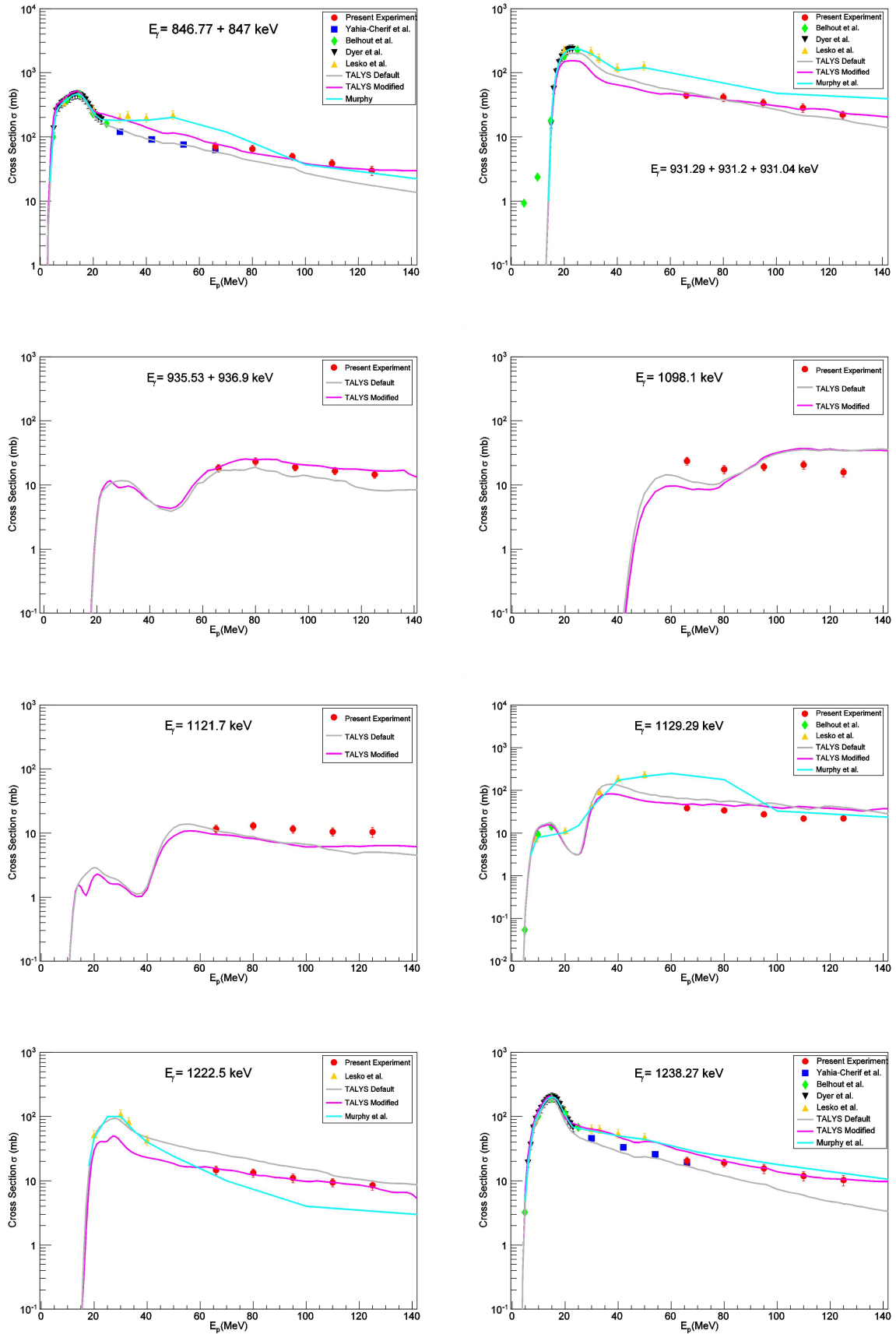


Fig. 10. Same as in Fig.5 but for 8 other  $\gamma$ -ray lines emitted in proton interactions with the  $^{56}\text{Fe}$  target

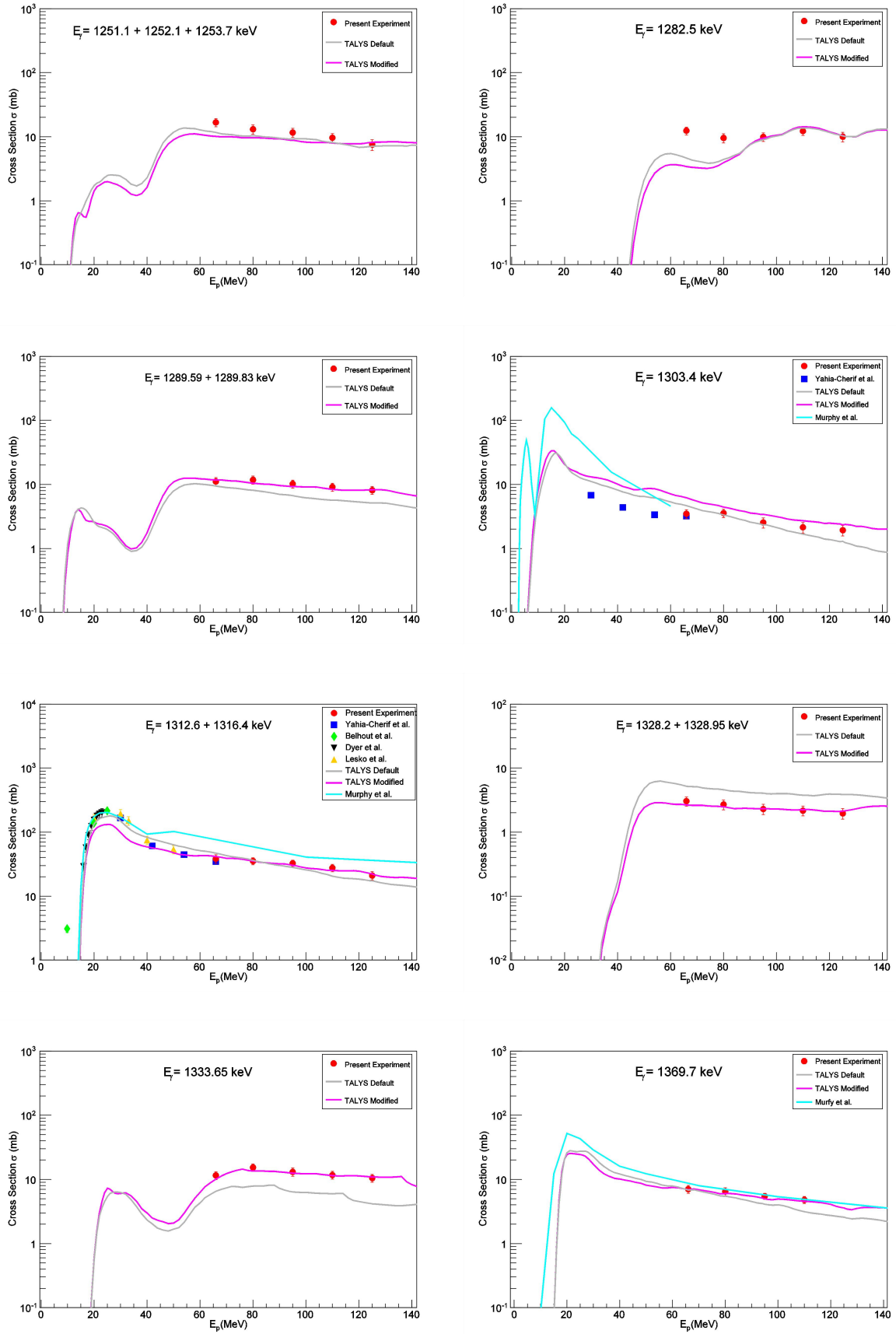


Fig.11. Same as in Fig.5 but for 8 other  $\gamma$ -ray lines emitted in proton interactions with the  $^{56}\text{Fe}$  target.

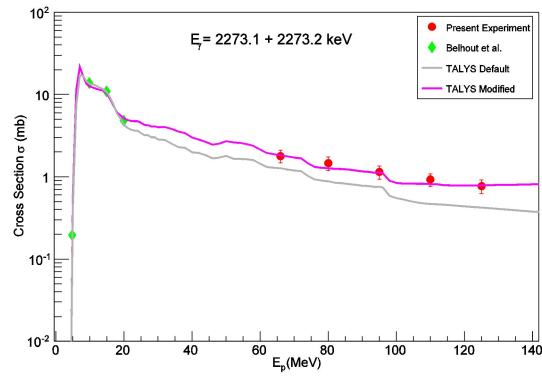
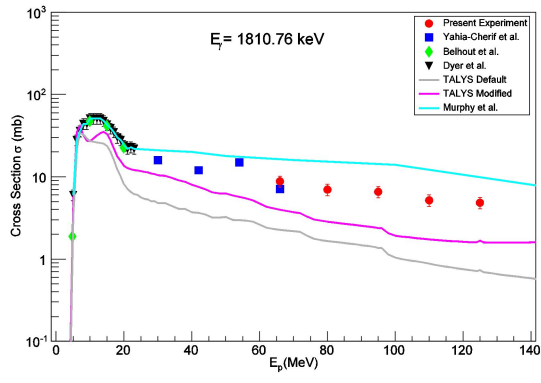
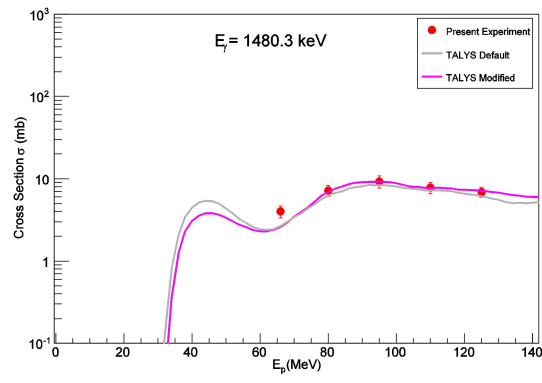
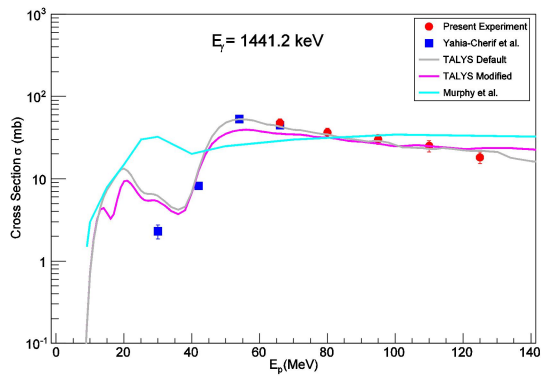
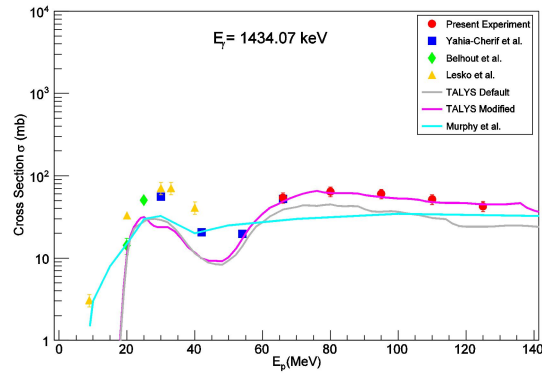
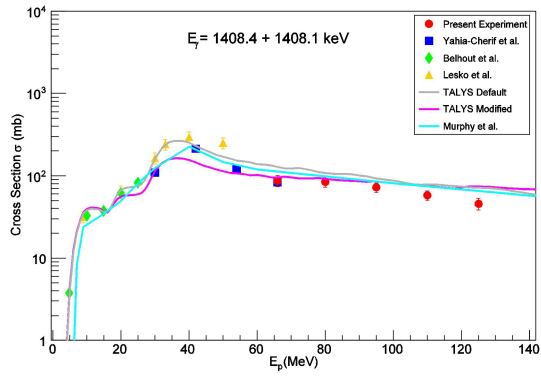


Fig. 12. Same as in Fig.5 but for 6 other  $\gamma$ -ray lines emitted in proton interactions with the  $^{56}\text{Fe}$  target.

Table 8. Experimental values of total production cross sections and their uncertainties for  $\gamma$ -ray lines emitted in proton irradiations with the  $^{nat}\text{Mg}$  target

$\gamma$ -ray energy (keV)	$E_p = 66$ MeV	$E_p = 80$ MeV	$E_p = 95$ MeV	$E_p = 110$ MeV	$E_p = 125$ MeV
331.91	7.13 ± 1.25	6.88 ± 1.23	6.64 ± 1.21	6.08 ± 1.07	5.03 ± 0.93
350.73	23.23 ± 3.26	21.78 ± 3.21	20.33 ± 3.16	18.44 ± 2.25	16.96 ± 2.56
389.71	2.06 ± 0.35	1.77 ± 0.30	1.49 ± 0.24	1.31 ± 0.23	1.19 ± 0.21
425.81	0.92 ± 0.13	0.71 ± 0.11	0.51 ± 0.08	0.36 ± 0.06	0.30 ± 0.05
439.99	35.55 ± 5.36	33.39 ± 4.86	31.22 ± 4.35	29.39 ± 4.36	27.15 ± 4.52
450.7	37.01 ± 4.56	35.89 ± 4.49	34.77 ± 4.42	31.24 ± 4.05	27.69 ± 4.05
472.2	4.06 ± 0.55	3.63 ± 0.46	3.21 ± 0.37	3.20 ± 0.35	2.73 ± 0.33
563.19	0.85 ± 0.14	0.79 ± 0.12	0.73 ± 0.12	0.76 ± 0.14	0.69 ± 0.13
585.03	34.22 ± 5.05	31.42 ± 4.76	28.62 ± 4.40	26.04 ± 3.74	23.38 ± 3.90
937	7.36 ± 1.06	7.02 ± 0.99	6.68 ± 0.92	6.46 ± 0.95	5.92 ± 0.97
974.74	2.20 ± 0.41	1.79 ± 0.33	1.39 ± 0.24	1.28 ± 1.99	1.04 ± 0.19
1016.9	2.77 ± 0.49	2.44 ± 0.46	2.11 ± 0.36	2.02 ± 0.37	1.66 ± 0.29
1368.63	56.53 ± 8.03	49.22 ± 7.03	41.90 ± 6.03	34.60 ± 4.81	29.53 ± 3.86
1808.68	5.28 ± 0.90	4.57 ± 0.80	3.86 ± 0.69	3.42 ± 0.59	2.76 ± 0.49
2754.02	12.05 ± 2.02	11.09 ± 1.94	10.12 ± 1.87	9.66 ± 1.63	9.44 ± 1.58

Table 9. Same as in Table 8 for  $\gamma$ -ray lines emitted in proton irradiations with the  $^{nat}\text{Si}$  target.

$\gamma$ -ray energy (keV)	$E_p = 66$ MeV	$E_p = 80$ MeV	$E_p = 95$ MeV	$E_p = 110$ MeV	$E_p = 125$ MeV
331.91	1.29 ± 0.22	1.99 ± 0.32	2.13 ± 0.32	2.32 ± 0.40	2.19 ± 0.30
350.73	6.59 ± 0.99	9.96 ± 1.46	10.98 ± 1.42	10.21 ± 1.53	10.59 ± 1.63
389.71	5.08 ± 0.74	4.86 ± 0.73	4.49 ± 0.57	3.70 ± 0.49	3.58 ± 0.49
416	30.54 ± 4.25	29.28 ± 3.92	25.03 ± 3.19	22.42 ± 3.27	19.58 ± 2.68
439.99	16.86 ± 2.87	13.64 ± 2.28	15.14 ± 2.47	13.77 ± 2.30	13.90 ± 2.32
450.7	10.32 ± 1.49	8.71 ± 1.35	8.36 ± 1.33	7.69 ± 1.28	6.42 ± 0.94
585.03	21.14 ± 3.42	21.37 ± 3.56	20.64 ± 3.04	18.77 ± 2.99	18.44 ± 2.88
780.8	14.57 ± 2.08	13.88 ± 1.99	13.81 ± 1.72	9.25 ± 1.18	10.92 ± 1.46
843.76	10.01 ± 1.46	9.12 ± 1.46	8.82 ± 1.24	7.51 ± 0.97	7.02 ± 1.11
890.87	3.81 ± 0.64	3.58 ± 0.59	3.54 ± 0.63	3.87 ± 0.67	3.41 ± 0.56
957.3	13.00 ± 1.59	12.25 ± 1.58	11.30 ± 1.37	11.08 ± 1.44	8.86 ± 1.12
974.74	4.82 ± 0.74	5.00 ± 0.83	4.66 ± 0.75	4.30 ± 0.67	3.78 ± 0.61
1273.36	7.83 ± 1.05	7.21 ± 1.15	6.92 ± 1.11	6.69 ± 1.13	6.57 ± 1.00
1368.63	44.03 ± 5.84	48.09 ± 6.05	45.59 ± 5.74	41.94 ± 5.46	43.58 ± 5.76
1778.97	61.85 ± 8.73	52.81 ± 7.32	43.70 ± 5.25	34.86 ± 4.30	30.08 ± 3.91

Table 10. Same as in Table 8 for  $\gamma$ -ray lines emitted in proton irradiations with the  $^{56}\text{Fe}$  target

$\gamma$ -ray energy (keV)	$E_p = 66$ MeV	$E_p = 80$ MeV	$E_p = 95$ MeV	$E_p = 110$ MeV	$E_p = 125$ MeV
126.95	12.46 $\pm$ 1.95	13.62 $\pm$ 2.41	12.83 $\pm$ 2.40	11.87 $\pm$ 1.90	9.15 $\pm$ 1.49
156.29	54.10 $\pm$ 6.57	52.89 $\pm$ 6.48	45.92 $\pm$ 6.61	41.31 $\pm$ 5.43	33.66 $\pm$ 5.24
211.98	28.89 $\pm$ 3.35	28 $\pm$ 2.75	23.81 $\pm$ 2.54	19.7 $\pm$ 2.27	16.16 $\pm$ 1.92
226.43	10.93 $\pm$ 1.21	9.96 $\pm$ 1.51	10.49 $\pm$ 1.52	11.14 $\pm$ 1.53	8.40 $\pm$ 1.26
274.8	8.99 $\pm$ 1.29	13.54 $\pm$ 1.97	10.76 $\pm$ 1.65	8.72 $\pm$ 1.28	7.40 $\pm$ 1.08
377.88	35.45 $\pm$ 5.09	33.75 $\pm$ 5.33	28.77 $\pm$ 3.47	25.13 $\pm$ 3.28	22.87 $\pm$ 3.10
411.9	31.72 $\pm$ 4.79	29.61 $\pm$ 4.49	24.68 $\pm$ 3.80	21.02 $\pm$ 2.88	17.96 $\pm$ 2.56
783.3	33.4 $\pm$ 5.42	25.72 $\pm$ 3.79	26.62 $\pm$ 4.28	29.06 $\pm$ 4.67	20.82 $\pm$ 3.62
846.77	70.90 $\pm$ 10.69	64.68 $\pm$ 9.54	49.33 $\pm$ 5.94	38.72 $\pm$ 5.53	29.82 $\pm$ 5.02
931.29	44.68 $\pm$ 5.32	41.4 $\pm$ 6.04	33.85 $\pm$ 5.15	28.39 $\pm$ 4.44	22.19 $\pm$ 2.96
935.53	18.36 $\pm$ 2.50	23.32 $\pm$ 3.23	18.95 $\pm$ 2.33	16.56 $\pm$ 2.17	14.57 $\pm$ 1.85
1098.1	23.71 $\pm$ 3.39	17.52 $\pm$ 2.61	19.16 $\pm$ 2.48	20.64 $\pm$ 3.04	15.78 $\pm$ 2.34
1121.7	11.66 $\pm$ 1.69	12.98 $\pm$ 1.69	11.61 $\pm$ 1.61	10.47 $\pm$ 1.56	10.42 $\pm$ 1.80
1129.9	38.55 $\pm$ 5.66	34.22 $\pm$ 4.50	27.38 $\pm$ 3.66	22.08 $\pm$ 2.76	22.22 $\pm$ 3.29
1222.5	14.69 $\pm$ 2.20	13.28 $\pm$ 1.91	11 $\pm$ 1.70	9.46 $\pm$ 1.35	8.48 $\pm$ 1.31
1238.27	20.39 $\pm$ 2.92	19.08 $\pm$ 2.50	15.51 $\pm$ 2.63	11.89 $\pm$ 1.87	10.21 $\pm$ 1.90
1252.1	16.65 $\pm$ 2.33	13.11 $\pm$ 2.17	11.63 $\pm$ 1.85	9.62 $\pm$ 1.53	7.51 $\pm$ 1.40
1282.5	12.40 $\pm$ 1.75	9.55 $\pm$ 1.53	9.93 $\pm$ 1.51	12.26 $\pm$ 1.82	9.98 $\pm$ 1.70
1289.83	11.11 $\pm$ 1.70	11.78 $\pm$ 1.70	10.21 $\pm$ 1.45	9.11 $\pm$ 1.30	8.14 $\pm$ 1.16
1303.4	3.48 $\pm$ 0.55	3.56 $\pm$ 0.54	2.53 $\pm$ 0.46	2.14 $\pm$ 0.41	1.93 $\pm$ 0.36
1316.04	38.27 $\pm$ 5.81	35.41 $\pm$ 4.57	32.49 $\pm$ 3.99	27.55 $\pm$ 3.68	21.00 $\pm$ 3.10
1328.2	3.04 $\pm$ 0.50	2.70 $\pm$ 0.47	2.30 $\pm$ 0.42	2.17 $\pm$ 0.38	1.96 $\pm$ 0.37
1333.65	11.51 $\pm$ 1.64	15.35 $\pm$ 2.06	13.13 $\pm$ 1.93	11.72 $\pm$ 1.63	10.46 $\pm$ 1.48
1369.7	7.05 $\pm$ 1.00	6.49 $\pm$ 0.95	5.47 $\pm$ 0.91	4.80 $\pm$ 0.62	
1408.4	87.04 $\pm$ 13.64	84.34 $\pm$ 11.96	72.29 $\pm$ 9.63	57.82 $\pm$ 7.62	45.56 $\pm$ 7.28
1434.07	54.21 $\pm$ 7.84	64.29 $\pm$ 8.85	60.36 $\pm$ 7.70	51.69 $\pm$ 7.13	42.71 $\pm$ 6.05
1441.2	47.79 $\pm$ 5.64	36.53 $\pm$ 4.61	30.17 $\pm$ 4.14	25.04 $\pm$ 3.94	18.2 $\pm$ 2.92
1480.3	4.01 $\pm$ 0.67	7.19 $\pm$ 1.10	9.28 $\pm$ 1.56	7.81 $\pm$ 1.21	5.89 $\pm$ 0.96
1810.76	8.81 $\pm$ 1.36	7.01 $\pm$ 1.13	6.57 $\pm$ 1.04	5.17 $\pm$ 0.83	4.85 $\pm$ 0.77
2273.2	1.79 $\pm$ 0.31	1.47 $\pm$ 0.28	1.15 $\pm$ 0.21	0.96 $\pm$ 0.16	0.77 $\pm$ 0.14

#### 4.4.1 Comparison to previous experimental data

In comparing the  $\gamma$ -ray line production cross section experimental data from this work (represented by red full circles in Figs. (5 – 12)) to previous counterparts, we considered the following series of data sets also reported in these figures:

- the data set measured by Dyer et al. [20] at the Washington university tandem accelerator up to  $E_p = 23$  MeV (shown in black, down-oriented full triangles),
- the data sets taken respectively by Benhabiles et al. [17] (shown in green circles) and Belhout et al. [24, 25] (green full diamonds) at the Orsay Paris-Saclay university tandem accelerator up to  $E_p = 26$  MeV,
- the data set taken by Lesko et al. [29] (yellow, up-oriented full triangles) at the Lawrence Berkeley Laboratory's Cyclotron accelerators over the proton energy range of  $E_p = 8.9 - 50$  MeV and
- our data set taken by Yahia-Cherif et al. [18] (blue full squares) at the SSC of iThemba LABS for  $E_p = 30 - 66$  MeV.

As can be seen in Figs. (5-12), the previous experimental data sets from Refs. (17, 20, 24, 25) are mainly concentrated within the low proton energy region, our previous data set [18] extends the data from other works over the proton energy range of  $E_p = 30 - 66$  MeV, while our results from the current work up-date and further extend the previous experimental data over the proton energy range of  $E_p = 66 - 125$  MeV. Our contributions, thus bringing additional substantial high-energy cross section data, are particularly important as they reduce the need for non-experimental extrapolation, then allowing to better identify the nuclear reaction mechanisms behind the  $\gamma$ -ray production in astrophysical environments.

Observing Figs. (5-12) reveals that the cross section experimental data from this work and Refs. [17, 18, 20, 24, 25] show to be mutually consistent. However, the cyclotron data set of Lesko et al. [29] appears to significantly deviate upward relative to the other previous data sets for most of the  $\gamma$ -ray lines having this data set reported.

One also notes that only our data sets from this work and from Ref. [18] are present in Figs. (5-12) for the majority of the  $\gamma$ -ray lines, these two data sets being mutually consistent within the involved experimental uncertainties. In case of other  $\gamma$ -ray lines, one observes that only the data set from the current work is reported.

Further observation of Figs. (5-12) shows that for the lines having previous experimental data reported (other than our previous data set [18]), located below and around the low proton energy compound resonance structure at  $E_\gamma = 20 - 40$  MeV, an overall consistency holds between our two experimental data sets and lower energy data from earlier works [17, 20, 24, 25], while the Lesko et al. [29] data set generally deviates upward from the other data sets, likely due to the consideration by these authors of more isotopes in the explored targets. Since the latter data set [29] was taken into account in the Murphy et al. semi-empirical compilation [31], it consequently affects, both in magnitude and in energy dependence, the trends of the  $\gamma$ -ray line excitation functions predicted by this database, as will be clarified in subsection 5.2.

For further details, we proceed below to comparing the various experimental data sets separately for each explored target.

#### **A. $\gamma$ -rays in proton reactions with the $^{nat}\text{Mg}$ target**

Among the cross section experimental results from the  $^{nat}\text{Mg}$  target presented in Figs. (5, 6), those for the three lines at  $E_\gamma = 563.2, 937.0$  and  $1016.9$  keV are reported here for the first time, to our knowledge. As can be observed in these figures, the cross section data often exhibit a gradual, more or less marked reduction as the proton beam energy increases beyond the double- bump compound resonance structure over the range of  $E_p \cong 30 - 50$  MeV. One

can also see that the current study significantly extends to higher proton energies the results from previous works [18, 20, 24, 25, 29] with maintaining a direct continuity with them. As can be checked in Table 1, the  $^{24}\text{Mg}$  is the most abundant isotope within the  $^{\text{nat}}\text{Mg}$  target relative to the  $^{25}\text{Mg}$  and  $^{26}\text{Mg}$  isotopes. The production cross sections for the  $\gamma$ -ray line at  $E_\gamma = 1808.68$  keV from  $^{26}\text{Mg}$  (E2 transition from the  $J_i^\pi = 2^+$ , 1<sup>st</sup> excited state of this isotope to its ground state ( $J_f^\pi = 0^+$ , see Table 2), show to be in excellent agreement with our experimental data sets from this work and Ref. [4]. Notice also that the previous data sets from Refs. [24, 25] for this line are not included in Figs. (5, 6) due to substantial contributions from the Al backing [25].

We also report in these figures the  $\gamma$ -ray production cross sections from the de-excitation of excited states in  $^{25}\text{Mg}$ . In particular, the  $\gamma$ -ray line at  $E_\gamma = 585.03$  keV (E2 transition from the  $1/2^+$ , 1<sup>st</sup> excited state to the  $5/2^+$  ground state), and two other lines at  $E_\gamma = 389.71$  and  $974.74$  keV resulting from the de-excitation of the 2<sup>nd</sup> excited state of this isotope (see Table 2). The analysis of the  $\gamma$ -ray line at  $585.03$  keV must account for the contribution of another transition at  $E_\gamma = 583.04$  keV, probably resulting from the de-excitation of the  $1^+$ , 1<sup>st</sup> excited state of  $^{22}\text{Na}$  to its  $3^+$  ground state. For the  $\gamma$ -ray transitions at  $E_\gamma = 389.71$  and  $974.74$  keV, our experimental results are in good agreement with our previous data set [18]. In case of the line  $E_\gamma = 585.03$  keV, our cross sections from the current work are consistent with the data sets from Refs. [24,25], but differ from our previous data set [18], which is higher by  $\approx 22\%$  at  $E_p = 66$  MeV.

Two  $\gamma$ -ray lines emitted by  $^{24}\text{Mg}$  were also investigated: the line at  $E_\gamma = 1368.63$  keV resulting from the decay of the 1<sup>st</sup> excited state to the ground state, and the line at  $E_\gamma = 2754.02$  keV (E2 transition from the  $4^+$ , 2<sup>nd</sup> excited state to the  $2^+$ , 1<sup>st</sup> excited state). The former line can be affected by another nearby line at  $E_\gamma = 1368.7$  keV attributed to the  $^{22}\text{Na}$  isotope (transition from the  $2^+$ , 2<sup>nd</sup> excited state to the  $1^+$ , 1<sup>st</sup> excited state). Although the short lifetime of the emitting state leads to a strongly Doppler-shifted and broadened  $\gamma$ -ray line expected to be hardly separated from its neighbor line from  $^{24}\text{Mg}$ , this contribution has been taken into account in our analysis (see Fig. 6). Comparing our  $\gamma$ -ray line production cross section data for these two lines to previous data, one observes a smooth extension of the latter to higher proton energies, along with an excellent agreement with the data sets from Refs. [20, 24, 25]. In contrast, the cross section data reported by Lesko et al. [29] are significantly higher than our cross section values, which can be attributed to the inclusion by these authors [29] of other isotopes in their target, then contributing to substantially enhance the cross sections at lower proton energies. Two other  $\gamma$ -ray lines at  $E_\gamma = 450.7$  and  $425.81$  keV emitted respectively by the  $^{23}\text{Mg}$  and  $^{24}\text{Al}$  isotopes during their decay to their ground states were also

analyzed. As shown in Fig. 6, our cross section data for these lines are in excellent agreement with our previous data set [18] and the previous data sets from Refs. [24, 25].

Other  $\gamma$ -ray lines attributed to the de-excitations of the 1<sup>st</sup> excited states of the  $^{21,23,24}\text{Na}$  isotopes were identified in the  $\gamma$ -ray energy spectra recorded from the  $^{\text{nat}}\text{Mg}$  target, for which the corresponding production cross sections were determined. These are the lines at  $E_\gamma = 331.91, 439.99, 472.7$  and  $563.19$  keV, the latter line being reported here for the first time. Our cross sections from the current work for these lines show mostly to be in good agreement with our previous data set [18] and the previous data sets from Refs. [18,24,25], except for the line at  $E_\gamma = 439.99$  keV for which our previous cross section data set [18] is higher by  $\approx 31\%$  than our data from the current work at  $E_p = 66$  MeV.

The production cross sections for the  $\gamma$ -ray line at  $E_\gamma = 937$  keV from the de-excitation of  $^{18}\text{F}$  and the line at  $E_\gamma = 1016.9$  keV from the de-excitation of  $^{23}\text{Ne}$  (also coming from  $^{22}\text{Na}$ , see Table 2) have been determined for the first time in this work, to our knowledge.

Finally, the  $\gamma$ -ray line production cross sections for the line at  $E_\gamma = 350.73$  keV, stemming from the decay of the 1<sup>st</sup> excited state of  $^{21}\text{Ne}$  to its ground state, were determined and compared with our previous data from Ref. [18]. A difference is observed between our current cross section data and our previous data [18], amounting to  $24.7\%$  at the proton energy of  $E_p = 66$  MeV.

### **B. $\gamma$ -rays in proton reactions with the $^{\text{nat}}\text{Si}$ target**

The proton irradiations of the  $^{\text{nat}}\text{Si}$  target led us to the identification of 15  $\gamma$ -ray lines. Their analysis indicates that they are predominantly produced in binary nuclear reactions involving the  $^{27}\text{Si}$ ,  $^{28}\text{Si}$ ,  $^{29}\text{Si}$ , and  $^{30}\text{Si}$  isotopes making up the natural Si target (see Table 3). The corresponding experimental production cross sections were determined and are compared in Figs. (7, 8) to previous counterparts from Refs. [18,20,17,29]. As in case of the  $^{\text{nat}}\text{Mg}$  target, one observes a progressive reduction of the production cross sections as the proton beam energy increases beyond the low energy region of compound resonances.

The production cross sections of the  $\gamma$ -ray line at  $E_\gamma = 1273.36$  keV, due to the de-excitation of the 1<sup>st</sup> excited state of  $^{29}\text{Si}$ , were determined. The previous data sets for this line, reported in Refs. [17,18], appear to be consistently extended to higher proton energies thanks to the current work.

The most intense line at  $E_\gamma = 1778.97$  keV, emitted in the de-excitation of  $^{28}\text{Si}$ , was also analyzed and its experimental production cross sections were determined. Previous experimental cross section data sets for this line have been reported in Refs. [17,18, 20,29]. The agreement between our data sets from this work and Ref. [18] is excellent at  $E_p = 66$

MeV. As can be seen, these results are consistent with the previous lower proton energy data sets from Refs. [17, 20], but are slightly higher than that reported by Lesko et al. [29].

Two main  $\gamma$ -ray lines at  $E_\gamma = 780.8$  and  $957.3$  keV emitted in the de-excitations of  $^{27}\text{Si}$  were analyzed (see Table 3). As shown in Fig. 8, our cross section data sets for these lines from this work and Ref. [18] are consistent with the Lesko et al. data [29].

Two  $\gamma$ -ray lines at  $E_\gamma = 416$  and  $843.76$  keV coming from the de-excitation of  $^{26,27}\text{Al}$  isotopes were observed and their production cross sections were determined, the second line being also fed by another transition at  $E_\gamma = 843.92$  keV from the  $^{26}\text{Al}$  isotope. A very good agreement is observed between our cross section data sets for these lines from this work and Ref. [18].

However, concerning the  $843.76$  keV line the previous cross section data set reported in Ref. [29] at proton energies above  $E_p = 30$  MeV appears to be higher and exhibiting a different energy dependence compared to the overall datasets.

The  $\gamma$ -ray production cross sections were determined for transitions from the de-excitation of the 1<sup>st</sup> two excited states of  $^{25}\text{Mg}$ , produced in proton binary reactions with the  $^{\text{nat}}\text{Si}$  target.

They concern the lines at  $E_\gamma = 389.71$ ,  $585.03$  keV and, for the first time, the line at  $E_\gamma = 974.74$  keV line (see Table 3). The  $585.03$  keV line overlaps with another line of very close energy located at  $E_\gamma = 583.04$  keV emitted during the de-excitation of  $^{22}\text{Na}$ . A very good agreement and a smooth continuity at high proton energies are observed between our data sets for these lines from this work and Ref. [18].

A line at  $E_\gamma = 1368.63$  keV from the  $^{24}\text{Mg}$  isotope was also observed and analyzed. As previously mentioned in the case of the  $^{\text{nat}}\text{Mg}$  target, another line with very close energy of  $E_\gamma = 1368.7$  keV, emitted by the  $^{22}\text{Na}$  isotope, is likely to overlap with this line of  $^{24}\text{Mg}$  (see Table 3). Our cross section data for this doublet are consistent with our previous data set [18], although the latter values are higher by about 30% to 40% relative to the proton lower energy data of Lesko et al. [29].

The  $\gamma$ -ray production cross sections were determined here for the first time for a second line at  $E_\gamma = 890.87$  keV from the  $^{22}\text{Na}$  isotope, for which no previous cross section data has been reported in the literature, to our knowledge.

We also determined the production cross sections for  $\gamma$ -ray lines emitted in the deexcitation of the 1<sup>st</sup> excited states of  $^{23}\text{Mg}$ ,  $^{21,23}\text{Na}$  and  $^{21}\text{Ne}$  isotopes, for which only our previous cross section data set [18] has been reported. These are the lines at  $E_\gamma = 450.7$  keV from  $^{23}\text{Mg}$ ,  $E_\gamma = 439.99$  keV from  $^{23}\text{Na}$ ,  $E_\gamma = 331.91$  keV from  $^{21}\text{Na}$ , and  $E_\gamma = 350.73$  keV from  $^{21}\text{Ne}$  (see Table 3). As can be seen in Fig. 8, an excellent agreement is observed between our two experimental cross section data sets for these lines from this work and Ref. [18].

### C. $\gamma$ -rays in proton reactions with the $^{56}\text{Fe}$ target

The iron target used in our experiments was highly enriched, to over 99%, in  $^{56}\text{Fe}$ . Figs. (9-12) report the production cross sections for 30  $\gamma$ -ray lines produced mainly in inelastic proton scattering. Our experimental data for the lines at  $E_\gamma = 125.95, 156.27, 211.98, 274.8, 377.88, 411.9, 846.77, 931.29, 1129.29, 1222.5, 1238.27, 1303.4, 1316.04, 1408.4, 1434.07, 1441.2, 1810.76$  and  $2273.1$  keV are compared in these figures to the previous experimental data sets reported in Refs. [18,20,24,25,29]. One observes that the experimental  $\gamma$ -ray production cross sections show a marked increase over the low proton energy region, reaching maxima approximately in the energy range of  $E_p = 10 - 60$  MeV. This behavior is characteristic of nuclear reactions dominated by the compound nucleus mechanism. Beyond this region, a gradual decrease in the  $\gamma$ -ray cross sections is observed with increasing the proton beam energy. This trend signs the transition to direct and pre-equilibrium nuclear reaction mechanisms, and successive openings of other competitive reaction pathways, such as the emission of nucleons and alpha particles, which reduces the probability of  $\gamma$ -ray line emission. The production cross sections for the other  $\gamma$ -ray lines at  $E_\gamma = 226.4, 783.3, 935.53, 1098.1, 1121.7, 1251.1, 1282.5, 1289.59, 1328.2, 1333.65, 1369.7$  and  $1480.3$  keV (see Table 4) are reported for the 1<sup>st</sup> time in this work, to our knowledge. As can be observed, our results show a clear continuity of the  $\gamma$ -ray production cross sections measured in this work with our previous data set [18] and the earlier data sets reported in Refs. [20, 24, 25, 29].

We determined the  $\gamma$ -ray production cross sections for the 1<sup>st</sup> three levels of the  $^{56}\text{Fe}$  mass spectral band. They correspond to the intense lines at  $846.77, 1238.27$  and  $1810.76$  keV emitted in the de-excitation of the 1<sup>st</sup> three excited states of  $^{56}\text{Fe}$ . Our cross section results for these lines show good agreement with our previous data set [18] and with the lower-energy data sets of Belhout et al. [24, 25] and Dyer et al. [20]. In contrast, the data set of Lesko et al. [29] appears to be systematically higher than the previous data sets for the lines at  $E_\gamma = 846.77$  and  $1238.27$  keV at proton beam energies above  $E_p = 30$  MeV.

The extraction of the integral cross section for the  $846.78$  keV  $\gamma$ -ray line was carried out through a careful and rigorous deconvolution procedure aiming at removing the neutron induced background and interfering adjacent line peaks. A multipeak Gaussian fitting procedure was indeed employed to separate the contributions from the line peaks at  $E_\gamma = 843.76$  keV from  $^{27}\text{Al}$  and  $E_\gamma = 848$  keV from  $^{52}\text{Cr}$ . The interfering Aluminium component arises from the inelastic scattering of secondary neutrons and protons off the AFRODITE reaction chamber constituent material. Similarly, in the fitting of the  $\gamma$ -ray line at  $1238.27$  keV, the contribution of a small spurious line peak at  $E_\gamma = 1241.7$  keV, attributed to the decay of

$^{53}\text{Mn}$ , was taken into account. Besides, the cross sections for the  $\gamma$ -ray lines at  $E_\gamma = 1303.4$  and  $2273.2$  keV, also coming from the decay of this isotope (de-excitations of the 10<sup>th</sup> and 7<sup>th</sup> excited states, respectively), were determined. The obtained results are consistent both with our previous data set [18] and the earlier data sets from Refs. [24, 25].

Gamma-ray lines originating from the decays of the  $^{53,54,55}\text{Fe}$  isotopes were also observed in the  $\gamma$ -ray energy spectra from the  $^{56}\text{Fe}$  target, and the corresponding production cross sections were determined. These are the lines at  $E_\gamma = 274.8, 1222.5, 1129.9$  keV and, for the 1<sup>st</sup> time, the lines at  $1328.2$  and  $1369.7$  keV (see Table 4).

Furthermore, production cross sections were determined for two  $\gamma$ -ray line doublets at  $E_\gamma = 411.9$  and  $1408.4$  keV attributed, respectively, to the de-excitation of the  $^{54}\text{Fe}$  and  $^{55}\text{Fe}$  isotopes.

The  $1316.4$  keV  $\gamma$ -ray line shows a low energy bump associated with a  $1312.2$  keV line, probably originating from  $^{56}\text{Fe}$ . Because of Doppler broadening, these two components could not be resolved. Then, their peak areas were combined (see Ref. [18]). The  $931.29$  keV  $\gamma$ -ray line is a triplet that may result from the de-excitation of the  $5/2^-$  excited state of  $^{55}\text{Fe}$  to its  $3/2^-$  state, in addition to the transitions :  $5^+ \rightarrow 7^+$  and  $8^+ \rightarrow 7^-$  in  $^{54}\text{Mn}$ .

It is always found that the  $\gamma$ -ray line production cross sections derived in this work show to be in good agreement with the previous experimental data reported in the literature, excepting the data set from Ref. [29]. In particular, this data set is distinguished by a significant discrepancy with other data for the  $\gamma$ -ray lines at  $E_\gamma = 931.29, 1129.9, 1222.5$  and  $1408.4$  keV, a difference becoming pronounced for incident proton beam energies above  $E_p = 30$  MeV. The  $\gamma$ -ray production cross sections for the lines at  $E_\gamma = 156.29, 211.98, 377.88$  and  $1441.2$  keV, resulting from the de-excitation of the  $^{53,54}\text{Mn}$  isotopes, and the  $125.95$  keV line coming from the de-excitation of  $^{55}\text{Mn}$  were determined and compared to our data from this work and from Ref. [18] and to the previous ones from Refs. [24, 25]. Very good agreements along with an excellent continuity with these data sets is observed.

The production cross sections for several new  $\gamma$ -ray lines have been determined in this work. This includes lines originating from the de-excitation of the  $^{52,53}\text{Mn}$  isotopes, particularly the lines at  $E_\gamma = 1253.7, 1121.7$  and  $1289.83$  keV, as well as six new lines at  $E_\gamma = 783.3, 935.53, 1098.1, 1282.5, 1333.65$  and  $1480.3$  keV from the decay of the  $^{50,51,52}\text{Cr}$  isotopes. In addition, the  $226.3$  keV line from  $^{50}\text{V}$  has been determined. These new  $\gamma$ -ray line production cross sections, reported in Table 4, then constitute a decisive experimental contribution to the existing database [31] and allow a better understanding of the  $\gamma$ -ray emission patterns. Finally, in case of the  $\gamma$ -ray line at  $E_\gamma = 1434.07$  keV emitted in the de-excitation of the 1<sup>st</sup> excited state of  $^{52}\text{Cr}$ , a good agreement is observed between our cross section experimental data from

the present work, our previous data set [18] and the previous data sets reported in Refs. [24, 25, 29].

#### 4.4.2 Comparison to the Murphy et al. semi-empirical compilation

In 2009, Murphy et al. [31] compiled the available experimental cross section data for about 140 main, intense  $\gamma$ -ray lines prominent in the SFs and ISM, resulting from the decay of low-lying excited states produced in nuclear reactions induced by light ions (protons,  $^3\text{He}^+$  ions and  $\alpha$ -particles) on target nuclei ranging from  $^4\text{He}$  to  $^{56}\text{Fe}$ . In particular, updating earlier databases for proton and  $\alpha$ -particle induced reactions, they extrapolated the existing experimental data to higher projectile energies up to several hundreds of MeV/u not covered by experiment, based on TALYS code [32] calculations. In addition, they provided predicted trends of  $\gamma$ -ray line excitation functions for weak lines produced during the decay of high-lying excited states, also based on TALYS code calculations.

The cross section excitation functions predicted by the Murphy et al. semi-empirical compilation [31] are also plotted in Figs. (5-12) for the sake of comparison to the integral  $\sigma(E_p)$  experimental data from the present and previous works [17, 18, 24, 25, 29].

Observing these figures, one first notes that the predicted cross section curves show an overall consistency with the experimental data sets regarding their proton energy dependence for most of the  $\gamma$ -ray lines, while they show significant deviations in magnitude from them in the presence of the Lesko et al. data set [29].

One also observes that, when it is present, the experimental cross section data set of Lesko et al. [29] (considered in the Murphy et al. compilation) is often significantly higher than the other experimental data for  $E_p \geq 30$  MeV probably due to the inclusion by these authors of more isotopes in the investigated targets.

One may thus expect that in case of the  $\gamma$ -ray lines having earlier experimental cross section data sets included in the Murphy et al. compilation [31] up to  $E_p \cong 50$  MeV (the highest proton energy in the Lesko et al. [29] data set), the predicted cross section curves should agree with the  $\sigma(E_p)$  experimental data in presence of the Lesko et al. data set [29]. However, this turns out to be true only in the case of two  $\gamma$ -ray lines at  $E_\gamma = 1368.63 + 1388.7$  keV (doublet) and  $E_\gamma = 1778.97$  keV produced in (p, p' $\gamma$ ) inelastic proton scattering off the  $^{\text{nat}}\text{Si}$  target.

Otherwise, variable observations hold corresponding to the facts that the predicted cross section curves from Ref. [31] either overestimate or underestimate the measured cross section data in the presence or the absence of the Lesko et al. data set.

As can be seen in Figs. (5-12), the cross section curves predicted by the Murphy et al. compilation [31] show to be in partial agreement with the experimental data in case of the lines at  $E_\gamma = 1808.68$  keV (in absence of the Lesko et al. data set [29]) from the  $^{nat}\text{Mg}$  target, at  $E_\gamma = 1368.63 + 1368.7$  keV (in presence of the Lesko et al. data set [29]), at  $E_\gamma = 1778.97$  keV (in presence of the Lesko et al. data set [29]) from the  $^{nat}\text{Si}$  target, and at  $E_\gamma = 1369.7$  keV (in absence of the Lesko et al. data set [29]) from the  $^{56}\text{Fe}$  target.

The predicted curves overestimate the experimental cross section data in the presence of the Lesko et al. data set [29] for the lines at  $E_\gamma = 1388.63 + 1388.7$  from the  $^{nat}\text{Mg}$  target, and  $E_\gamma = 846.77 + 847$  keV,  $E_\gamma = 931.29 + 931.2 + 931.04$  keV (triplet),  $E_\gamma = 1129.29$  keV,  $E_\gamma = 1238.27$  keV,  $E_\gamma = 1312.26 + 1318.4$  keV keV,  $E_\gamma = 1408.4 + 1408.1$  keV from the  $^{56}\text{Fe}$  target.

They also overestimate the cross section experimental data sets even in the absence of the Lesko et al. [29] data set in case of the two lines at  $E_\gamma = 1303.4$  keV,  $E_\gamma = 1810.78$  keV from the  $^{56}\text{Fe}$  target.

In contrast, the predicted curves by the Murphy et al. compilation [31] underestimate the cross section experimental data sets in the absence of the Lesko et al. [29] data set in case of the  $\gamma$ -ray lines at  $E_\gamma = 439.99$  keV,  $E_\gamma = 450.7$  keV and  $E_\gamma = 2754.12$  keV from the  $^{nat}\text{Mg}$  target, and  $E_\gamma = 411.4 + 411.9$  keV from the  $^{56}\text{Fe}$  target.

They also underestimate the cross section experimental data sets in the presence of the data set of the Lesko et al. [29] in case of the  $\gamma$ -ray lines at  $E_\gamma = 780.8$  keV,  $E_\gamma = 843.76 + 843.92$  keV,  $E_\gamma = 957.3$  keV from the  $^{nat}\text{Si}$  target, and  $E_\gamma = 1222.5$  keV,  $E_\gamma = 1434.7$  keV from the  $^{56}\text{Fe}$  target.

## 5 Interpretation within the nuclear reaction theory, TALYS code calculations

For interpreting and validating the experimental  $\gamma$ -ray line production cross sections, we compare them in this section to counterparts derived by TALYS code [32] calculations in terms of the predictions of nuclear reaction theory versus the incident energy domains covered by the accelerated protons.

This code allows calculating theoretical cross sections for nuclear reactions induced by  $\gamma$ -rays, neutrons and charged particles (p, d, t,  $^3\text{He}^+$ ,  $\alpha$ -particles) on various target nuclei over the incident energy range of  $E_{\text{lab}} = 1$  keV - 250 MeV, based on reaction mechanisms (compound nucleus, direct, pre-equilibrium, fusion-evaporation reactions, fission, etc.) expected to occur over this incident energy region. It has been extensively used earlier by

several groups for calculating nuclear cross sections for prompt and delayed  $\gamma$ -ray lines prominent in SFs and the ISM emitted in proton and  $\alpha$ -particle induced reactions on stable and radioactive nuclei (see Refs.[18, 36] and Refs therein). It contains intrinsic nuclear data libraries (for masses, level densities, discrete states, OMPs,  $\beta_\lambda$  level deformation parameters,  $\gamma$ -ray branching ratios, strength functions, etc.) and default built-in parameters based on phenomenological or microscopic models. Alternatively, the user is allowed to introduce one's own input data (such as OMPs, nuclear level deformation parameters, etc.) referred to as modified TALYS code parameters that can be derived from theoretical models or the analysis of experimental data. This can be done using keywords provided in TALYS or the code's intrinsic nuclear data libraries.

Integrating several nuclear reaction models, this code proves to be a powerful tool for nuclear data prediction and analysis [16]. Enabling comparisons between its predictions and experimental data with allowing model adjustments, it provides predictions of nuclear observables over energy intervals that have not been explored experimentally. Several research groups have checked its efficiency and accuracy via comparing its predictions with experimental data for a variety of nuclear reactions [16, 17, 18, 30, 36, 38].

At very low energies, nuclear reactions generally involve neutrons as projectiles due to the repulsive Coulomb barrier for charged particles, the dominant reaction mechanisms being elastic scattering and capture processes. As the incident energy increases and inelastic scattering channels open, the reactions proceed through compound nucleus formation and direct reaction mechanisms. The latter are described by the Distorted Waves Born Approximation (DWBA) for spherical nuclei and the coupled channel reactions model in case of deformed nuclei. At higher energies, pre-equilibrium mechanisms and multiple particle emission become predominant. In this context, TALYS ensures a gradual transition between these different reaction mechanisms, thus enabling reliable modeling over a wide energy range where one or more mechanisms may simultaneously contribute depending on the considered physical conditions.

For the  $\gamma$ -ray emission, TALYS distinguishes two types of nuclear levels: (i) the 1<sup>st</sup> type corresponding to low-excitation, discrete nuclear levels that de-excite exclusively by  $\gamma$ -ray emission taken from the RIPL library [51], and (ii) a 2<sup>nd</sup> type of higher-excitation levels, treated statistically using energy bins that group a large number of states. The latter levels are handled through a continuous level density rather than considered as individual states in order to account for their high density and collective behavior.

There exist several versions of the TALYS code, which is still under development. In the current work, we used the 1.96 version [32].

In a first step, we calculated theoretical  $\gamma$ -ray line cross section excitation functions using the default parameters of TALYS, with introducing only the incident energy values and the mass and atomic numbers of the projectiles and targets. The obtained results are reported in Figs (5 - 12) together with the measured cross section data.

Observing Figs (5 – 12), one first notes a gradual decrease in the calculated  $\gamma$ -ray production cross sections as the incident energy increases beyond the low energy region dominated by compound nucleus resonances, due to the successive openings of other competitive nuclear reaction channels. For the majority of the  $\gamma$ -ray lines, this trend is well followed by the experimental data. As can be seen, at some exceptions the calculated excitation functions account reasonably well for the energy dependence of the experimental data for most of the  $\gamma$ -ray lines. In some cases, they also account partially even quantitatively for the measured cross section data. This holds for the lines at  $E_\gamma = 331.91, 439.99, 472.2, 937, 1016.8 + 1016.9, 1368.63 + 1368.7$  keV from the  $^{nat}\text{Mg}$  target,  $E_\gamma = 416.85, 450.7 + 451.7$  keV from the  $^{nat}\text{Si}$  target, and  $E_\gamma = 125.95, 156.27, 211.98, 274.8, 847.77 + 847, 931.29 + 931.2 + 931.04, 1238.27, 1312.6 + 1318.4, 1441.2, 1480.3$  keV from the  $^{56}\text{Fe}$  target. However, the calculated excitation functions show substantial discrepancies relative to the experimental data for several  $\gamma$ -ray lines.

Indeed, while at very low energies satisfactory agreements are observed between the calculated cross sections and experimental data, significant differences appear elsewhere over a wide energy range. This led us to modify the default input parameters in TALYS so that the calculated cross sections reproduce as well as possible the experimental data. For doing this, we treated each nucleus separately by implementing different options in the code associated with each involved reaction mechanism, consistently with the nature of the target nucleus. Particular attention was paid to the  $\gamma$ -ray lines resulting from the de-excitation of the 1<sup>st</sup> excited states of certain nuclei. These transitions are important because they are often well defined and allow for reliable comparisons between different experiments. This is the case, e.g., for the  $\gamma$ -ray lines at  $E_\gamma = 350.73, 1368.63, \text{ and } 1808.68$  keV from the  $^{nat}\text{Mg}$  target, the lines at  $E_\gamma = 843.76, 1368.63, \text{ and } 1778.97$  keV from the  $^{nat}\text{Si}$  target, and the lines at  $E_\gamma = 846.77, 1238.27, 1316.04, 1408.4, \text{ and } 1434.07$  keV from the  $^{56}\text{Fe}$  target.

In the TALYS code, the contribution of the compound nucleus mechanism is mainly described by the Hauser-Feshbach's statistical model including width fluctuation corrections according to the Moldauer approach [52]. Direct reactions are treated within the framework of

the DWBA approach through the ECIS-06 code [53]. Concerning the pre-equilibrium reactions, TALYS mainly uses the two-component exciton model developed by C. Kalbach [54]. The fitting of the parameters associated with these different reaction mechanisms shows that no significant differences is observed between the TALYS code predictions and the experimental data. These mechanisms are correctly formulated and implemented in TALYS. The modifications that produce a remarkable improvement and allow a better reduction of the discrepancy between the TALYS predictions and the cross section experimental data mainly concern the OMP and the  $\beta_\lambda$  level deformation parameters. This is due to the fact that the TALYS code considers the nucleus as deformed, and that the calculations of the total  $\gamma$ -ray line production cross sections are performed using the deformed OMPs.

Then, in a second step, we performed TALYS code [32] calculations of the total  $\gamma$ -ray line cross sections with introducing our own modified OMPs and  $\beta_\lambda$  level deformation parameters in the code source, aiming to improve the agreements between the predicted theoretical excitation functions and the experimental data. This was done following the method detailed in our previous paper [18] reporting similar cross section results for the same targets of  $^{\text{nat}}\text{Mg}$ ,  $^{\text{nat}}\text{Si}$ , and  $^{56}\text{Fe}$  explored over the proton beam energy range of  $E_p = 30 - 66$  MeV. For extracting these parameters, we have priorily analyzed tens of angular distribution experimental data for elastic and inelastic nucleon scatterings off the  $^{24,25,26}\text{Mg}$ ,  $^{28,29,30}\text{Si}$  and  $^{54,56}\text{Fe}$  isotopes taken from the literature, e.g., from the IAEA's EXFOR library [55]. Then, we used the coupled-channels reactions code OPTMAN [56] available in the RIPL-3 data library [57] to generate comprehensive theoretical fits to the angular distribution experimental data for deriving our own modified OMPs and  $\beta_\lambda$  level deformation parameters. The form of the energy dependent interaction potential is given in Ref. [56]. In addition to optimizing the OMPs, this required us adjusting the nuclear level density parameters and the coupling schemes of  $\gamma$ -ray emitting residual isotopes listed in tables (2, 3, 4).

Another important improvement made concerns the inclusion in the calculations of many  $\gamma$ -ray line production cross sections, and of contributions from multiple particle emission such as the  $(p, p\gamma \ ^3\text{He})$  and  $(p, 2n^3\text{He})$  reactions. These reactions produce the same  $\gamma$ -ray lines as the  $(p, p')$  inelastic scattering and play a significant role, particularly at high incident energies. Their contributions have been neglected in the previous calculations. Tables 11 and 12 report, respectively, the optimized modified OMP and  $\beta_\lambda$  level deformation parameters used in our TALYS code calculations.

The calculated  $\gamma$ -ray production excitation functions using our OMPs and  $\beta_\lambda$  level deformation parameters are also plotted (by solid pink curves) in Figs. (5 – 12) for

comparison to the cross section experimental data from the present and previous works [17, 18, 20, 24, 25, 29]. As can be seen, they generally stand close to the cross section curves generated in our calculations using the default parameters of TALYS. Not surprisingly, the two calculation modes lead to mutually consistent trends of the cross section curves regarding their evolving proton energy dependences. However, more or less marked departures between the two sets of calculated cross section values are observed for several  $\gamma$ -ray lines with increasing the proton beam energy beyond the resonant structures at  $E_p = 20 - 40$  MeV. Finally, one observes that significant improvements of the agreement between the calculated excitation functions using our modified OMPs and  $\beta_\lambda$  level deformation parameters and our experimental data (including our previous data set [18]) are obtained for most of the  $\gamma$ -ray lines, reaching good to excellent consistency in case of the lines at  $E_\gamma = 331.91, 350.73, 472.2, 583.04 + 583.03, 937 + 583.03, 1808.68$  keV from the  $^{nat}\text{Mg}$  target,  $E_\gamma = 389.71, 416.85, 450.7 + 451.7, 583.04 + 585.03, 843.76 + 843.92, 974.74, 1388.63 + 1388.7, 1778.87$  from the  $^{nat}\text{Si}$  target, and  $E_\gamma = 125.95, 156.27, 211.98, 274.8, 377.88, 411.4 + 411.9, 846.77 + 847, 931.29 + 931.2 + 931.04, 935.53 + 936.9, 1222.5, 1238.27, 1251.1 + 1252.1 + 1253.7, 1289.59 + 1289.83, 1312.6 + 1316.4, 1328.2 + 1328.95, 1333.05, 1369.7, 1408.4 + 1408.1, 1434.07, 1441.2, 1420.3, 2273.1, 2273.2$  from the  $^{56}\text{Fe}$  target.

Below, we further discuss these cross section results with considering separately the  $\gamma$ -ray lines produced in the proton irradiation of each target system.

#### A. $\gamma$ -ray lines in proton reactions with the $^{nat}\text{Mg}$ target

In Figures 5 - 6, the solid pink curves represent the sum of the contributions from all isotopes composing the  $^{nat}\text{Mg}$  target. These figures clearly show that the use of our modified OMP and  $\beta_\lambda$  level deformation parameters considerably improve the reproduction of the experimental data both in absolute value and in energy dependence over the entire investigated proton energy range. Especially for the lines at  $E_\gamma = 1808.68$  keV (of  $^{26}\text{Mg}$ ),  $585.03$  and  $974.74$  keV ( $^{25}\text{Mg}$ ),  $472.2$  keV ( $^{24}\text{Na}$ ),  $331.92$  keV ( $^{21}\text{Na}$ ),  $1016.9$  keV ( $^{23}\text{Ne}$ ),  $350.73$  keV ( $^{21}\text{Ne}$ ) and  $937$  keV ( $^{18}\text{F}$ ).

Furthermore, for the six lines at  $E_\gamma = 389.71$  keV ( $^{25}\text{Mg}$ ),  $1368.63$  and  $2754.02$  keV ( $^{24}\text{Mg}$ ),  $450.7$  keV ( $^{23}\text{Mg}$ ),  $425.81$  ( $^{24}\text{Al}$ ) and  $439.99$  keV ( $^{23}\text{Na}$ ), the agreement between the calculated cross section values and experimental data is in general quite good. A certain competition is observed between the calculations performed using the default TALYS parameters and those made with our modified parameters. For the lines at  $E_\gamma = 389.71, 1368.63$  and  $425.81$  keV, the calculated values with our modified parameters are higher than

those generated with the TALYS default parameters, while the opposite is observed for the lines at  $E_\gamma = 450.7$  and  $439.99$  keV. Concerning the line at  $E_\gamma = 2754.02$  keV, the calculated values with the default parameters are higher for incident energies of  $E_p < 60$  MeV, while those calculated using our own modified parameters are higher over the remaining proton energy range. It is important to highlight the significant contribution of the  $^{24}\text{Mg}(p, x)^{22}\text{Na}$  reaction in the evaluation of the final cross sections for the  $\gamma$ -ray lines at  $E_\gamma = 583.04$ ,  $1368.7$ , and  $1016.8$  keV.

However, both the excitation curves generated using the TALYS default parameters and our modified parameters are unable to reproduce the experimental data for the line at  $E_\gamma = 563.19$  keV ( $^{24}\text{Na}$ ), that shows significant discrepancies between the calculated and measured cross section values.

Table 11. Adjusted values of our OMP parameters used as modified inputs in our TALYS calculations for proton induced reactions with  $^{24,25,26}\text{Mg}$ ,  $^{28,29,30}\text{Si}$  and  $^{56}\text{Fe}$ .

OMP Parameters	$^{56}\text{Fe}$	$^{28,30}\text{Si}$	$^{29}\text{Si}$	$^{24,26}\text{Mg}$	$^{25}\text{Mg}$
$E_f$ (MeV)	-6.96	-7.16	-7.16	-7.16	-6.18
$r_c$ (fm)	1.361	1.324	1.324	1.324	1.324
$r_v$ (fm)	1.282	1.190	1.160	1.184	1.196
$a_v$ (fm)	0.665	0.552	0.669	0.562	0.592
$V_1$ (MeV)	60.2	51.2	51.2	50.3	60.5
$V_2$ (MeV $^{-1}$ )	0.0082	0.0051	0.0055	0.0053	0.0055
$V_3$ (MeV $^{-2}$ )	0.000033	0.000022	0.000018	0.000022	0.000017
$W_1$ (MeV)	14.2	14.0	15.0	14.0	14.0
$W_2$ (MeV)	75.0	75.0	75.0	75.0	75.0
$r_{vd}$ (fm)	1.290	1.190	1.160	1.184	1.196
$a_{vd}$ (fm)	0.585	0.522	0.590	0.562	0.592
$d_1$ (MeV)	15.0	14.6	12.5	14.6	14.6
$d_2$ (MeV $^{-1}$ )	0.0580	0.0216	0.0216	0.0216	0.0216
$d_3$ (MeV)	10.00	11.10	11.10	11.10	11.10
$r_{vso}$ (fm)	1.000	1.123	1.007	1.078	1.078
$a_{vso}$ (fm)	0.580	0.757	0.746	0.815	0.580
$V_{sol}$ (MeV)	8.1	7.7	7.9	7.7	9.7
$V_{so2}$ (MeV $^{-1}$ )	0.0090	0.0035	0.0035	0.0035	0.0035
$W_{sol}$ (MeV)	-3.1	-4.5	-4.5	-4.2	-3.1
$W_{so2}$ (MeV)	160.0	332.0	160.0	223.0	160.0

Table 12. Adjusted values of the deformation parameters  $\beta_\lambda$  for proton reactions with  $^{24,25,26}\text{Mg}$ ,  $^{28,29,30}\text{Si}$  and  $^{56}\text{Fe}$  used as modified input in the TALYS calculations.

$\beta_\lambda$ deformation parameters	$^{24}\text{Mg}$	$^{25}\text{Mg}$	$^{26}\text{Mg}$	$^{28}\text{Si}$	$^{29}\text{Si}$	$^{30}\text{Si}$	$^{56}\text{Fe}$
$\beta_2$	0.758	0.554	0.449	-0.419	-0.320	0.315	0.141
$\beta_4$	-0.037	0.152	0.182	0.108	0.250	0.220	0.001

### B. $\gamma$ -ray lines in proton reactions with the $^{nat}\text{Si}$ target

As in case of the  $^{nat}\text{Mg}$  target, the continuous pink curves shown in Figures 7 - 8 represent the sum of the contributions from the  $^{28}\text{Si}$ ,  $^{29}\text{Si}$ , and  $^{30}\text{Si}$  isotopes constituting the natural  $^{nat}\text{Si}$  target. All the  $\gamma$ -ray lines from this target correspond to transitions from the 1<sup>st</sup> excited state to the ground state, except for the 389.71 keV line of  $^{25}\text{Mg}$ , which corresponds to a transition from the 2<sup>nd</sup> to the 1<sup>st</sup> excited state.

The excitation functions for the lines from the  $^{nat}\text{Si}$  target at  $E_\gamma = 1778.97$  ( $^{28}\text{Si}$ ), 843.76 ( $^{27}\text{Al}$ ), 416 ( $^{26}\text{Al}$ ), 389.71 and 585.03 ( $^{25}\text{Mg}$ ), 1368.63 keV ( $^{24}\text{Mg}$ ), calculated using our modified OMP and  $\beta_\lambda$  level deformation parameters, show excellent agreement with the entire set of experimental data, both in terms of the absolute values and the energy dependence over the whole investigated proton energy range. A similar observation holds for the line at  $E_\gamma = 450.7$  keV ( $^{23}\text{Mg}$ ), especially when the contribution of the  $\gamma$ -ray line at  $E_\gamma = 451.7$  keV, originating from the de-excitation of the 1<sup>st</sup> excited state of  $^{25}\text{Al}$ , is also taken into account, which had not been considered in previous studies.

In the case of the two new lines at  $E_\gamma = 974.74$  keV ( $^{25}\text{Mg}$ ) and 890.87 keV ( $^{22}\text{Na}$ ), the excitation functions calculated using our modified parameters are in very good agreement with the experimental data, fitting them very satisfactorily. For the lines located at  $E_\gamma = 439.99$  (from  $^{23}\text{Na}$ ), 331.91 ( $^{21}\text{Na}$ ), and 350.73 keV ( $^{21}\text{Ne}$ ), the calculated excitation functions using our modified input parameters show good overall agreement with the experimental data, correctly reproducing their absolute values for proton energies above 80 MeV. Conversely, for the lines of  $^{27}\text{Si}$  at  $E_\gamma = 780.8$  and 957.3 keV, the calculated excitation functions using our modified parameters show reasonable agreement with previous experimental data at proton energies below 45 MeV [18,29], but deviate significantly from the measured data for higher energies.

The only exception to the good results obtained in our study of the  $\gamma$ -ray lines from this target concerns the line of  $^{29}\text{Si}$  at  $E_\gamma = 1273.36$  keV; for this line, the calculations performed using our modified parameters and with the default parameters of TALYS show significant discrepancies with respect to the experimental data.

### C. $\gamma$ -ray lines in proton reactions with the $^{56}\text{Fe}$ target

Figures 9–12 show that the performed TALYS code calculations using our modified OMPs as well as the  $\beta_\lambda$  level deformation parameters for most of the  $\gamma$ -ray lines produced in proton induced reactions on the  $^{56}\text{Fe}$  target provide theoretical excitation functions that describe very well the experimental data sets.

For the fifteen lines located at  $E_\gamma = 846.77, 1238.27, 2273.02$  ( $^{56}\text{Fe}$ ),  $274.8, 411.9, 931.29, 1222.5, 1316.04, 1408.4$  ( $^{55}\text{Fe}$ ),  $377.88, 1441.2$  ( $^{53}\text{Mn}$ ),  $156.29, 211.98$  ( $^{54}\text{Mn}$ ),  $125.95$  ( $^{55}\text{Mn}$ ) and  $1434.07$  ( $^{52}\text{Cr}$ ) keV an excellent agreement is observed between the cross section theoretical values and the experimental data over the entire incident proton energy range. The calculated  $\gamma$ -ray production cross sections for these transitions reproduce very well both our experimental data and those reported in References [18,20,24,25]. However, divergences are sometimes noted between these experimental data sets and those reported in Reference [29]. For the two  $\gamma$ -ray lines located at  $E_\gamma = 1303.4$  ( $^{56}\text{Fe}$ ) and  $1129.9$  ( $^{54}\text{Fe}$ ) keV, the theoretical values also show, in general, a good agreement with the experimental data. However, for the line at  $E_\gamma = 1303.4$  keV, the calculated values appear to be slightly higher than both our experimental data and the reference data reported in [18]. A similar observation is also valid for the line at  $E_\gamma = 1129.9$  keV; however, in this case, the calculations performed with the TALYS code reproduce very well the reference data reported in [24,25]. For the seven new lines at energies  $E_\gamma = 935.53, 1333.65$  ( $^{52}\text{Cr}$ ),  $1253.7$  ( $^{52}\text{Mn}$ ),  $1289.83$  ( $^{53}\text{Mn}$ ),  $1328.2$  ( $^{53}\text{Fe}$ ),  $1369.7$  ( $^{56}\text{Fe}$ ) and  $1480.3$  ( $^{51}\text{Cr}$ ) keV, an excellent agreement is also observed between the calculated excitation functions using our modified parameters and our experimental data, both in absolute values and in energy dependences. Thus, for the four new lines at energies  $E_\gamma = 1121.7$  ( $^{53}\text{Mn}$ ),  $783.3, 1098.1$  and  $1282.5$  ( $^{50}\text{Cr}$ ) keV, the calculated cross sections using our modified input parameters overestimate our experimental data without showing any significant improvement compared to the calculations performed with the TALYS default parameters. It should be noted that the good results obtained for the two lines at  $E_\gamma = 931.29$  et  $1253.7$  keV are achieved when the contribution of two other distinct transitions having the same energy for each line is taken into account, as indicated in Table 4. These contributions had not been considered in previous studies. It should be also noted that additional contributions for some lines are well predicted by our calculations using the modified parameters: see, e.g., the lines at  $E_\gamma = 2273.2, 411.9$  and  $1316.04$  keV.

The cross sections for the line at  $E_\gamma = 266.3$  keV correspond to the sum of two components: one arises from the de-excitation of the 1<sup>st</sup> excited state of  $^{50}\text{V}$ , while the second is associated with the de-excitation of a far excited state of  $^{54}\text{Mn}$  at  $E_x = 4998.1$  keV toward a lower excited level. The calculations performed with the TALYS code for this line do not provide satisfactory results, since they fail to compute the cross sections corresponding to the contribution from  $^{54}\text{Mn}$ . At last, significant discrepancies are observed between the values calculated using our modified input parameters and the entire set of experimental data for the line at  $E_\gamma = 1810.76$  keV ( $^{56}\text{Fe}$ ), while the cross sections calculated with the default parameters considerably underestimate the experimental data.

Finally, the predicted theoretical excitation functions for the three targets of  $^{nat}\text{Mg}$ ,  $^{nat}\text{Si}$  and  $^{56}\text{Fe}$  explored in this work show an overall good agreement with the experimental data, despite some observed discrepancies. These differences may be attributed to various possible causes, such as the influence of secondary reactions or the presence of impurities within the targets. The obtained results contribute to the enrichment of existing nuclear databases, which are essential both for practical applications and for theoretical studies, then providing a significant contribution to the understanding of the nuclear reactions investigated.

## 6 Potential applications, conclusions and perspectives

### A. Applications in nuclear physics and applied sciences

Ground-based measurements of nuclear  $\gamma$ -ray line production cross sections are essential for a wide range of applications in nuclear physics, astrophysics,  $\gamma$ -ray astronomy, and space sciences ([12], [18], [26], [31]).

The experimental cross section data sets obtained in this work and previous studies ([18], [36-39]), measured at the SSC of iThemba LABS, span a broad proton energy range extending from  $E_p = 30$  up to 200 MeV. An experimental data set, taken over the proton energy range of  $E_p = 125 - 200$  MeV, is currently under treatment.

These data sets, collected for solid targets of  $^{nat}\text{C}$ , Mylar ( $^{12}\text{C} + ^{16}\text{O}$ ),  $^{nat}\text{Mg}$ ,  $^{nat}\text{Si}$ ,  $^{40}\text{Ca}$ , and  $^{56}\text{Fe}$ , elements abundant in astrophysical environments such as SFs and the ISM, will significantly update and enrich nuclear databases, especially the Murphy et al. compilation ([31]).

This allows further applications particularly in nuclear reaction theory, nuclear astrophysics and  $\gamma$ -ray astronomy for addressing various questions needing the knowledge of these observables and of the total  $\gamma$ -ray line emission fluxes ([12, 18, 26]).

In nuclear physics and related applied sciences, the new experimental nuclear  $\gamma$ -ray line production cross sections can allow to reliably improve many research topics. Primarily, modern theoretical nuclear reaction codes such as TALYS [32], EMPIRE 2 [58] and OPTMAN [56] can be improved and updated, notably for evaluating the OMPs, needed nuclear structure data, and modeling nuclear interactions. They can be used for optimizing and benchmarking nuclear reaction models, particularly over the transition region between compound nucleus resonant and pre-equilibrium reactions (see, e.g.[18, 36] and references therein).

Besides, these data sets can be useful in Ion Beam Analysis (IBA) for Particle-Induced Gamma-ray Emission (PIGE) studies to perform non-destructive and depth profiling analyses

in Materials science and Archeology. Furthermore, they can be of great interest in the tests and development of experimental fusion reactors where, e.g., accurate experimental data for the  $^{56}\text{Fe}$  isotope are needed in the modeling of activation, radiation damage and shielding of steel-based plasma facing structural materials.

In Medical physics, the proton-induced radiation therapy can benefit of the new nuclear  $\gamma$ -ray line production cross sections for in vivo range verification (IVRV). Indeed, during the proton therapy of cancer, prompt  $\gamma$ -ray lines are emitted as the protons induce nuclear reactions inside the human tissues with Magnesium and Iron composing bones and biological structures. These high energy  $\gamma$ -ray cross section data sets can also be exploited in prompt  $\gamma$ -ray imaging (PGI) where they can be directly introduced in Monte Carlo simulation codes, such as GANT4 [45], which ensures real-time, millimeter-level spatial monitoring of exactly where the therapeutic proton beam stops inside the patient's body.

## **B. Astrophysical implications**

In an other hand, precise knowledge of nuclear  $\gamma$ -ray line cross sections over the proton energy range of  $E_p = 30 - 200 \text{ MeV/n}$  is important in many astrophysical and space science issues, including :

- (i) **Solar Flares and the ISM:** Mg, Si, and Fe, known as "alpha and iron-peak elements," are highly abundant in astrophysical sites like SFs and the ISM. The new  $\gamma$ -ray cross sections can be directly used to model nuclear processes underlying solar flares, enabling studies of flare dynamics, composition, and the acceleration and energy spectra of flare-accelerated protons ([1-8], [12], [16], [18], [26], [31], [36], [50], [59], [60]).
- (ii) **Gamma-Ray Line Diagnostics:** Prominent  $\gamma$ -ray lines (e.g., the 6129 keV from  $^{16}\text{O}$ , 1369 keV from  $^{24}\text{Mg}$ , 1779 keV from  $^{28}\text{Si}$ , and 847 keV from  $^{56}\text{Fe}$ ) are produced in cosmic-ray interactions with ISM constituents. Line shape analyses ([36], [50], [59]) provide crucial information on the properties of ISM dust grains.
- (iii) **Interpretation of Space Mission Data:** The cross section data are crucial for interpreting high-energy observations from past and future NASA and ESA missions ([1]-[8], [60]-[62]), such as e-ASTROGAM, FERMI, INTEGRAL, and SMM.
- (iv) **Cosmic Ray Studies:** Accurate  $\gamma$ -ray line cross sections help model the interactions of low-energy cosmic rays (LECRs) with interstellar dust and gas,

providing insights into elemental abundances and cosmic-ray intensity in the galaxy ([12], [60], [74]).

- (v) **Stellar Nucleosynthesis:** The data support a better understanding of the production, destruction, and spallation of intermediate-mass elements in astrophysical sites ([63], [64], [73]).
- (vi) **Supernovae and Radioactive Decay Chains:** Measurements of  $\gamma$ -ray lines from isotopes such as  $^{56}\text{Ni}$ ,  $^{56}\text{Co}$ , and  $^{56}\text{Fe}$  allow direct observation of nucleosynthesis in supernovae and calculation of synthesized iron-peak element masses ([60], [64]-[66]).
- (vii) **Solar Flare and Space Weather Diagnostics:** The Sun behaves as a particle accelerator, initiating nuclear de-excitation lines and neutron capture signatures (e.g., the 2.223 MeV line from neutron capture on hydrogen), which are used to infer solar cosmic ray properties and photospheric density ([67]-[71]).
- (viii) **ISM Evolution and Steady-State Nucleosynthesis:** Long-lived radioactive isotopes such as  $^{26}\text{Al}$  (1.809 MeV line,  $T_{1/2} = 7 \times 10^5$  years) and  $^{60}\text{Fe}$  (1.173 and 1.333 MeV lines,  $T_{1/2} = 2.62 \times 10^6$  years) serve as clocks to trace chemical enrichment and ongoing nucleosynthesis in the galaxy ([72], [73], [60]).
- (ix) **Planetary Geochemistry Mapping:**  $\gamma$ -ray spectrometers on planetary orbiters (e.g., Mars Odyssey, MESSENGER) use these cross sections to map the elemental composition of planetary surfaces ([75], [76]).
- (x) **Classical Novae and Kilonovae:** Precision cross section data support modeling of radioactive decay lines (e.g.,  $^{18}\text{F}$ 's 511 keV annihilation flash, r-process elements in kilonovae) that power the light curves of these explosive events ([77], [78]).
- (xi) **Gamma-Ray Bursts (GRBs):** Laboratory  $\gamma$ -ray production cross sections are relevant for interpreting the prompt and afterglow emission spectra of GRBs ([3], [79], [80]).

## C Conclusion and Perspectives

The experimental results presented in this work represent a significant advancement for the scientific community. They provide updated and enriched nuclear databases, improve the modeling of nuclear reactions, and address fundamental questions in astrophysics and applied physics. The forthcoming analysis of the highest energy data ( $E_p = 125\text{--}200$  MeV) will further complete this work and open new areas, particularly for interpreting  $\gamma$ -ray observations of the Universe and developing innovative technologies in medical physics and nuclear engineering.

In summary, the precise knowledge of  $\gamma$ -ray production cross sections is a cross-disciplinary tool at the intersection of fundamental physics, astrophysics, medicine, and engineering. It will continue to play a key role in understanding and exploiting nuclear phenomena both on Earth and in the Universe.

## References

- [1] The e-ASTROGAM Collaboration, De Angelis, A., Tatischeff, V. et al., Exploring the extreme Universe with gamma rays in the MeV – GeV range, The e-ASTROGAM mission. *Exp Astron* 44, 25–82 (2017). <https://oi.org/10.1007/s10686-017-9533-6>
- [2] The e-ASTROGAM Collaboration, Vincent Tatischeff, Alessandro De Angelis et al, e-ASTROGAM mission: a major step forward for gamma-ray polarimetry, *Journal of Astronomical Telescopes, Instruments, and Systems*, Vol. 4, Issue 1, 011003 (November 2017). <https://doi.org/10.1117/1.JATIS.4.1.011003>
- [3] A. Abdo, M. Ackermann, A. Mea: Fermi observations of GRB 090902b: a distinct spectral component in the prompt and delayed emission. *Astrophys. J.* 706(1), L138 (2009) ; M. Ackermann, M. Ajello, A. Albert, A. Allafort, L. Baldini, G. Barbiellini, D. Bastieri, K. Bechtol, R. Bellazzini, E. Bissaldi, et al., High-energy gamma-ray emission from solar flares: summary of Fermi large area telescope detections and analysis of two M-class flares, *Astrophys. J.* 787(1) (2014) 15.
- [4] R.J. Murphy, R. Ramaty, B. Kozlovsky, Solar Abundances from Gamma-Ray Spectroscopy: Comparisons with Energetic Particle, Photospheric, and Coronal Abundances, *AIP Conference Proceedings*, vol.232, American Institute of Physics, 1991, pp.439–444.
- [5] G.H. Share, R.J. Murphy, Accelerated and ambient He abundances from gamma-ray line measurements of flares, *Astrophys. J.* 508(2) (1998) 876.
- [6] R.C. Lin, S. Krucker, G.J. Hurford, D.M. Smith, H.S. Hudson, G.D. Holman, R.A. Schwartz, B.R. Dennis, G.H. Share, R.J. Murphy, et al., RHESSI observations of particle acceleration and energy release in an intense solar gamma-ray line flare, *Astrophys. J.* 595(2) (2003) L69.
- [7] J. Kiener, M. Gros, V. Tatischeff, G. Weidenspointner, Properties of the energetic particle distributions during the October 28, 2003 solar flare from INTEGRAL/SPI observations, *Astron. Astrophys.* 445(2) (2006) 725–733.
- [8] M.J. Harris, V. Tatischeff, J. Kiener, M. Gros, G. Weidenspointner, High resolution  $\gamma$ -ray spectroscopy of flares on the East and West limbs of the Sun, *Astron. Astrophys.* 461(2) (2007) 723–729.

- [9] R. Ramaty, R.A. Schwartz, S. Enome, H. Nakajima, Gamma-ray and millimeter-wave emissions from the 1991 June X-class solar flares, *Astrophys. J.* 436 (1994) 941–949.
- [10] R.J. Murphy, B. Kozlovsky, G.H. Share, X.-M. Hua, R.E. Lingenfelter, Using gamma-ray and neutron emission to determine solar flare accelerated particle spectra and composition and the conditions within the flare magnetic loop, *Astrophys. J. Suppl. Ser.* 168(1) (2007) 167.
- [11] A.S.L. Sironi, Relativistic reconnection: an efficient source of non-thermal particles, *Astrophys. J. Lett.* 783(1) (2014) L21.
- [12] H. Benhabiles-Mezhoud, J. Kiener, V. Tatischeff and A.W. Strong, Erratum: “Deexcitation nuclear gamma-ray line emission from low-energy cosmic rays in the inner Galaxy” (2013, *ApJ*, 763, 98), *Astrophys. J.* 766(2) (2013) 139.
- [13] T. Vieu, S. Gabici, V. Tatischeff, Non-linear particle reacceleration by multiple shocks, *Mon. Not. R. Astron. Soc.* 510(2) (2022) 2529–2537.
- [14] R. Ramaty, B. Kozlovsky, R.E. Lingenfelter, Nuclear gamma-rays from energetic particle interactions, *Astrophys. J. Suppl. Ser.* 40 (1979) 487–526.
- [15] B. Kozlovsky, R. Murphy, R. Ramaty, Nuclear deexcitation gamma-ray lines from accelerated particle interactions, *Astrophys. J. Suppl. Ser.* 141(2) (2002) 523.
- [16] R.J. Murphy, B. Kozlovsky, J. Kiener, G.H. Share, Nuclear gamma-ray de-excitation lines and continuum from accelerated-particle interactions in solar flares, *Astrophys. J. Suppl. Ser.* 183(1) (2009) 142.
- [17] H. Benhabiles-Mezhoud, J. Kiener, J.-P. Thibaud, V. Tatischeff, I. Deloncle, A. Coc et al., Measurements of nuclear  $\gamma$ -ray line emission in interactions of protons and  $\alpha$ -particles with N, O, Ne, and Si, *Phys. Rev. C* 83(2) (2011) 024603 ;
- [18] W. Yahia-Cherif, S. Ouichaoui, J. Kiener, E.A. Lawrie, J.J. Lawrie, V. Tatischeff, A. Belhout, D. Moussa, P. Papka, H. Benhabiles-Mezhoud, et al., Measurement and analysis of nuclear  $\gamma$ -ray production cross sections in proton interactions with Mg, Si, and Fe nuclei abundant in astrophysical sites over the incident energy range  $E = 30\text{--}66$  MeV, *Phys. Rev. C* 102(2) (2020) 025802.
- [19] W.T. Vestrand, G.H. Share, R.J. Murphy, D.J. Forrest, E. Rieger, E.L. Chupp, G. Kanbach, The solar maximum mission atlas of gamma-ray flares, *Astrophys. J. Suppl. Ser.* 120(2) (1999) 409.
- [20] P. Dyer, D. Bodansky, A.G. Seamster, E.B. Norman, D.R. Maxson, Cross sections relevant to gamma-ray astronomy: proton induced reactions, *Phys. Rev. C* 23(5) (1981) 1865.
- [21] J. Narayanaswamy, P. Dyer, S.R. Faber, S.M. Austin, Production of 6.13-MeV gamma rays from the  $^{16}\text{O}(p, p\gamma)^{16}\text{O}$  reaction at 23.7 and 44.6 MeV, *Phys. Rev. C* 24(6) (1981) 2727.

- [22] A.G. Seamster, E.B. Norman, D.D. Leach, P. Dyer, D. Bodansky, Cross sections relevant to gamma-ray astronomy: alpha-particle-induced reactions, *Phys. Rev. C* 29(2) (1984) 394.
- [23] P. Dyer, D. Bodansky, D.D. Leach, E.B. Norman, A.G. Seamster, Cross sections relevant to gamma-ray astronomy: alpha-particle-induced reactions on  $^{12}\text{C}$ ,  $^{14}\text{N}$ , and  $^{16}\text{O}$  nuclei, *Phys. Rev. C* 32(6) (1985) 1873.
- [24] A. Belhout, J. Kiener, A. Coc, J. Duprat, C. Engrand, C. Fitoussi, M. Gounelle, A. Lefebvre-Schuhl, N. De Séréville, V. Tatischeff, et al.,  $\gamma$ -ray production by proton and  $\alpha$ -particle induced reactions on  $^{12}\text{C}$ ,  $^{16}\text{O}$ ,  $^{24}\text{Mg}$ , and Fe, *Phys. Rev. C* 76(3) (2007) 034607.
- [25] A. Belhout, J. Kiener, A. Coc, J. Duprat, C. Engrand, C. Fitoussi, M. Gounelle, A. Lefebvre-Schuhl, N. De Séréville, V. Tatischeff, et al., Erratum:  $\gamma$ -ray production by proton and  $\alpha$ -particle induced reactions on  $^{12}\text{C}$ ,  $^{16}\text{O}$ ,  $^{24}\text{Mg}$ , and Fe [*Phys. Rev. C* 76, 034607 (2007)], *Phys. Rev. C* 80(2) (2009) 029902.
- [26] H. Benhabiles-Mezhoud, Calcul du spectre total de l'émission gamma induite par interactions nucléaires des particules du rayonnement cosmique avec le milieu interstellaire et comparaison avec les observations de l'astronomie gamma, Ph.D. thesis, Paris 11, 2010.
- [27] J. Kiener, A. Belhout, V. Tatischeff, H. Benhabiles-Mezhoud, in: Proceedings of the DAE Symposium on Nuclear Physics, vol.53, Bhabha Atomic Research Centre, Roorkee, India, 2008.
- [28] J. Kiener, M. Berheide, N.L. Achouri, A. Boughrara, A. Coc, A. Lefebvre, F. de Oliveira Santos, C. Vieu,  $\gamma$ -ray production by inelastic proton scattering on  $^{16}\text{O}$  and  $^{12}\text{C}$ , *Phys. Rev. C* 58(4) (1998) 2174.
- [29] K.T. Lesko, E.B. Norman, R.-M. Larimer, S. Kuhn, D.M. Meekhof, S.G. Crane, H.G. Bussell, Measurements of cross sections relevant to  $\gamma$ -ray line astronomy, *Phys. Rev. C* 37(5) (1988) 1808.
- [30] J. Kiener, J. Bundesmann, I. Deloncle et al.,  $\gamma$ -ray emission in  $\alpha$ -particle interactions with C, Mg, Si, and Fe at  $E = 50 - 90$  MeV, *Phys. Rev. C* 104(2) (2021) 024621.
- [31] R.J. Murphy, B. Kozlovsky, J. Kiener, G.H. Share, Nuclear gamma-ray de-excitation lines and continuum from accelerated-particle interactions in solar flares, *Astrophys. J. Suppl. Ser.* 183(1) (2009) 142.
- [32] A.J. Koning, S. Hilaire, M.C. Duijvestijn, TALYS-1.0, in: International Conference on Nuclear Data for Science and Technology, EDP Sciences, 2007, pp.211–214 ; A.J. Koning, S. Hilaire, and S. Goriely. "TALYS: modeling of nuclear reactions." *The European Physical Journal A* 59.6 (2023): 1-85.
- [33] J. Sharpey-Schafer, Laboratory portrait: iThemba laboratory for accelerator-based sciences, *Nucl. Phys. News* 14(1) (2004) 5–13. [34] R. Newman, J. Lawrie, B. Babu, M.S.

- Fetea, S.V. Förtsch, S. Naguleswaran, J.V. Pilcher, D.A. Raave, C. Rigollet, J. Sharpey-Schafer, C.J. Stevens, F.D. Smit, G.F. Steyn, C.V. Wikner, D.G. Aschman, R. Beetge, R.W. Fearick, G. Mabala, S. Murray, N.J. Ncapayi, High-spin studies with the AFRODITE array, 1998.
- [35] M. Lipoglavšek, A. Likar, M. Vencelj, T. Vidmar, R.A. Bark, E. Gueorguieva, F. Komati, J.J. Lawrie, S.M. Maliage, S.M. Mullins, et al., Measuring high-energy  $\gamma$ -rays with Ge clover detectors, Nucl. Instrum. Methods Phys. Res., Sect. A, Accel. Spectrom. Detect. Assoc. Equip. 557(2) (2006) 523–527.
- [36] Y. Rahma, S. Ouichaoui, J. Kiener, E. A. Lawrie et al., Nuclear Physics A 1032 (2023) 122622, [www.elsevier.com/locate/nuclphysa](http://www.elsevier.com/locate/nuclphysa)
- [37] S. Ouichaoui, Y. Rahma, J. Kiener, E. A. Lawrie et al., 28th International Nuclear Physics Conference (INPC 2022), Journal of Physics: Conference Series 2586 (2023) 012099, IOP Publishing, <https://doi:10.1088/1742-6596/2586/1/012099>
- [38] Y. Rahma, S. Ouichaoui, J. Kiener, E. A. Lawrie et al., 28th International Nuclear Physics Conference (INPC 2022), Journal of Physics: Conference Series 2586 (2023) 012099, IOP Publishing, <https://doi:doi:10.1088/1742-6596/2586/1/012098>
- [39] W. Yahia Cherif, S. Damache, S. Ouichaoui, J. Kiener, E. A. Lawrie et al., Optical model potential parameter optimization for nucleon induced reactions on  $^{40}\text{Ca}$ : Implications on  $\gamma$ -ray production cross sections for residual Argon nuclei, EPJ Web of Conferences 322, 05004 (2025) CNR\*24, <https://doi.org/10.1051/epjconf/202532205004>
- [40] G. Duchêne, F.A. Beck, P.J. Twin, G. De France, D. Curien, L. Han, C.W. Beausang, M.A. Bentley, P.J. Nolan, J. Simpson, The clover: a new generation of composite Ge detectors, Nucl. Instrum. Methods Phys. Res., Sect. A, Accel. Spectrom. Detect. Assoc. Equip. 432(1) (1999) 90–110.
- [41] M. Lipoglavšek, A. Likar, M. Vencelj, T. Vidmar, R.A. Bark, E. Gueorguieva, F. Komati, J.J. Lawrie, S.M. Maliage, S.M. Mullins, et al., Measuring high-energy  $\gamma$ -rays with Ge clover detectors, Nucl. Instrum. Methods Phys. Res., Sect. A, Accel. Spectrom. Detect. Assoc. Equip. 557(2) (2006) 523–527.
- [42] J. Cresswell, J. Sampson, 2010•nnsa.dl.ac.uk, Mtsort language-edoc 033, 2010.
- [43] ROOT-CERNLIB, <https://root.cern.ch/>
- [44] R. C. Radford, <https://radware.phy.ornl.gov/>
- [45] S. Agostinelli, J. Allison, K. Amako, J. Apostolakis, H. Araujo, P. Arce, M. Asai, D. Axen, S. Banerjee, G. Barrand, et al., GEANT4-a simulation toolkit, Nucl. Instrum. Methods Phys. Res., Sect. A, Accel. Spectrom. Detect. Assoc. Equip. 506(3) (2003) 250–303.
- [46] M.E. Rose, The analysis of angular correlation and angular distribution data, Phys. Rev. 91(3) (1953) 610.

- [47] C. Iliadis, Nuclear Physics of Stars, John Wiley & Sons, 2007.
- [48] G. Gilmore, Practical Gamma-Ray Spectroscopy, 2nd edition, John Wiley & Sons, New York, 2008.
- [49] R.L. Bunting, J.J. Kraushaar, Short-lived radioactivity induced in Ge (Li) gamma-ray detectors by neutrons, Nucl. Instrum. Methods 118(2) (1974) 565–572.
- [50] J. Kiener, Shape and angular distribution of the 4.439-MeV  $\gamma$ -ray line from proton inelastic scattering off  $^{12}\text{C}$ , Phys. Rev. C 99(1) (2019) 014605.
- [51] R. Capote, M. Herman, P. Obložinský, P. G. Young, S. Goriely, T. Belgya, A. V. Ignatyuk, A. J. Koning, S. Hilaire, V. A. Plujko *et al.*, Nuclear Data Sheets 110, 3107 (2009).
- [52] P. A. Moldauer, Physical Review C 14, 764 (1976).
- [53] J. Raynal, CEA SaclayreportCEA-N-2772 (1994).
- [54] J. Raynal, CEA SaclayreportCEA-N-2772 (1994).
- [55] V.V. Zerkin and B. Pritychenko. Nucl. Instrum. Methods Phys. Res. A 888, 31 (2018), <https://doi.org/10.1016/j.nima.2018.01.045>
- [56] E.S. Soukhovitski *et al.*, OPTMAN code v1. <https://www-nds.iaea.org/RIPL-3/codes/OPTMAN/>
- [57] RIPL-3 library, <https://www-nds.iaea.org/RIPL-3/>
- [58] M. Herman, R. Capote, B. Carlson, P. Obložinský, M. Sin, A. Trkov, H. Wienke, and V. Zerkin, Nucl. Data Sheets 108, 2655 (2007).
- [59] Vincent Tatischeff, Jurgen Kiener,  $\gamma$ -ray lines from cosmic-ray interactions with interstellar dust grains, New Astronomy Reviews 48 (2004) 99–103.
- [60] Siegert, T., Calore, F., Jean, P. *et al.*  $\gamma$ -Ray Lines – Signatures of Nucleosynthesis, Cosmic Rays, Positron Annihilation, and Fundamental Physics. *Space Sci Rev* 222, 34 (2026). <https://doi.org/10.1007/s11214-026-01281-y>
- [61] [https://science.nasa.gov/ems/12\\_gamma-rays/](https://science.nasa.gov/ems/12_gamma-rays/)
- [62] [https://www.esa.int/Science\\_Exploration/Space\\_Science/Integral/Why\\_do\\_we\\_observe\\_gamma\\_rays](https://www.esa.int/Science_Exploration/Space_Science/Integral/Why_do_we_observe_gamma_rays)
- [63] Thomas Rauscher, Friedrich-Karl Thielemann, Karl-Ludwig Kratz, Nuclear level density and the determination of thermonuclear rates for astrophysics, Phys. Rev. C 56, 1613 – Published 1 September, 1997 ; <https://doi.org/10.1103/PhysRevC.56.1613>
- [64] <https://www.mpa-garching.mpg.de/27937/stellar-astrophysics-old>
- [65] De Angelis, A., Tatischeff, V., Argan, A. *et al.* Gamma-ray astrophysics in the MeV range. *Exp Astron* 51, 1225–1254 (2021). <https://doi.org/10.1007/s10686-021-09706-y>

[66] [https://www.mpg.de/8383537/supernova\\_gamma\\_ray\\_lines](https://www.mpg.de/8383537/supernova_gamma_ray_lines)

[67] <https://space-science.llnl.gov/research/gamma-ray-spectrometers>

[68] V. A. Dogiel<sup>1,2</sup> - V. Tatischeff<sup>3</sup> - K. S. Cheng<sup>4</sup> - D. O. Chernyshov<sup>1,2,4,5</sup> - C. M. Ko<sup>2</sup> - W. H. Ip<sup>2</sup>, Nuclear interaction gamma-ray lines from the Galactic center region, *A&A* 508, 1-7 (2009)

[69] Lu-Yao Jiang 1,2, Yun Wang 1, Yu-Jia Wei 1,2,3,4, Da-Ming Wei 1,2,✉, Xiang Li 1,2, Hao-Ning He 1,2, Jia Ren 1, Zhao-Qiang Shen 1, Zhi-Ping Jin, Probable evidence for a transient mega-electron volt emission line in the GRB 221023A, *Communications*. 2025 Mar 18;16:2668. doi: [10.1038/s41467-025-57791-w](https://doi.org/10.1038/s41467-025-57791-w)

[70] Andrea Francesco Battaglia<sup>1</sup>\* and Säm Krucker, New insights into the proton precipitation sites in solar flares, *A&A*, 694, A58 (2025).

[71] E. Tirado-Bueno 1, J. E. Mendoza-Torres 2 and C. Amador-Meléndez, High-Energy Neutron Enhancements Not Classified as GLEs: A Case Study Using Ground-Based Neutron Monitor Data, *Revista Mexicana de Astronomía y Astrofísica*, 61, 233-239, (2025).

[72] A. Casanovas-Hoste, C. Domingo-Pardo, J. Lereendegui-Marco<sup>4</sup>, C. Guerrero<sup>4</sup>, A. Tarifeño-Saldivia<sup>2</sup>, M. Krtićka<sup>5</sup>, M. Pignatari<sup>6,7,8,9</sup>, F. Calviño<sup>1</sup>, D. Schumann<sup>10</sup> et al. (nTOF Collaboration),

[73] De Angelis, A., Tatischeff, V., Argan, A. *et al.* Gamma-ray astrophysics in the MeV range. *Exp Astron* 51, 1225–1254 (2021). <https://doi.org/10.1007/s10686-021-09706-y>

[74] Bialy, S. Cold clouds as cosmic-ray detectors. *Commun Phys* 3, 32 (2020).

<https://doi.org/10.1038/s42005-020-0293-7>

[75] Jack T. Wilson ,\* David J. Lawrence , and Patrick N. Peplowski, Vincent R. Eke and Jacob A. Kegerreis, Space-based measurement of the neutron lifetime using data from the neutron spectrometer, *PHYSICAL REVIEW RESEARCH* 2, 023316 (2020),

<https://doi.org/10.1103/PhysRevResearch.2.023316>

[76] Randall K. Smith, Nancy S. Brickhouse, Chapter Four - Atomic Data Needs for Understanding X-ray Astrophysical Plasmas, *Advances In Atomic, Molecular, and Optical Physics*

Volume 63, 2014, Pages 271-321, <https://doi.org/10.1016/B978-0-12-800129-5.00004-3>

[77] Siegert, T., Calore, F., Jean, P. *et al.* -Ray Lines – Signatures of Nucleosynthesis, Cosmic Rays, Positron Annihilation, and Fundamental Physics. *Space Sci Rev* 222, 34 (2026).

<https://doi.org/10.1007/s11214-026-01281-y>

[78] Thomas Siegert, Sohan Ghosh, Kalp Mathur, Ethan Spraggon and Akshay Yeddanapudi, Nucleosynthesis constraints through  $\gamma$ -ray line measurements from classical novae.

Hierarchical model for the ejecta of <sup>22</sup>Na and <sup>7</sup>Be, *A&A*, Vol. 650 (2021) A187,

<https://doi.org/10.1051/0004-6361/202140300>

[79] Amina Trabelsi, Mourad Fouka, Saad Ouichaoui and Amel Belhout, Modeling of the Gamma Ray Burst photospheric emission : Monte Carlo simulation of the GRB prompt emission, numerical results and discussion, *Astrophysics and Space Science* (2024) 369:102,

<https://doi.org/10.1007/s10509-024-04366-8>

[80] Yassine Rahmani, Abdelaziz Sid, Mourad Fouka, Saad Ouichaoui and Redouane Mecheri, Multibands fitting of Gamma-ray burst's afterglow's light curves using the synchrotron external forward shock model, *Astrophysics and Space Science* (2024) 369:15, <https://doi.org/10.1007/s10509-024-04279-6>